



University of the  
West of England

# **Innovative Optical Non-contact Measurement of Respiratory Function Using Photometric Stereo**

Jahanzeb Ahmad

A thesis submitted in partial fulfilment of the requirements of the University of the  
West of England, Bristol, UK for the degree of Doctor of Philosophy

Faculty of the Environment and Technology  
University of the West of England, Bristol, UK

January 2015

# Abstract

Pulmonary functional testing is very common and widely used in today's clinical environment for testing lung function. The contact based nature of a Spirometer can cause breathing awareness that alters the breathing pattern, affects the amount of air inhaled and exhaled and has hygiene implications. Spirometry also requires a high degree of compliance from the patient, as they have to breathe through a hand held mouth piece. To solve these issues a non-contact computer vision based system was developed for Pulmonary Functional Testing. This employs an improved photometric stereo method that was developed to recover local 3D surface orientation to enable calculation of breathing volumes.

Although Photometric Stereo offers an attractive technique for acquiring 3D data using low-cost equipment, inherent limitations in the methodology have served to limit its practical application, particularly in measurement or metrology tasks. Traditional Photometric Stereo assumes that lighting directions at every pixel are the same, which is not usually the case in real applications and especially where the size of object being observed is comparable to the working distance. Such imperfections of the illumination may make the subsequent reconstruction procedures used to obtain the 3D shape of the scene, prone to low frequency geometric distortion and systematic error (bias). Also, the 3D reconstruction of the object re-

sults in a geometric shape with an unknown scale. To overcome these problems a novel method of estimating the distance of the object from the camera was developed, which employs Photometric Stereo images without using other additional imaging modality. The method firstly identifies the Lambertian Diffused Maxima regions to calculate the object's distance from the camera, from which the corrected per-pixel light vector is derived and the absolute dimensions of the object can be subsequently estimated. We also propose a new calibration process to allow a dynamic (as an object moves in the field of view) calculation of light vectors for each pixel with little additional computational cost. Experiments performed on synthetic as well as real data demonstrate that the proposed approach offers improved performance, achieving a reduction in the estimated surface normal error by up to 45% as well as the mean height error of reconstructed surface of up to 6 mm. In addition, compared with traditional photometric stereo, the proposed method reduces the mean angular and height error so that it is low, constant and independent of the position of the object placement within a normal working range.

A high (0.98) correlation between breathing volume calculated from Photometric Stereo and Spirometer data was observed. This breathing volume is then converted to absolute amount of air by using distance information obtained by

Lambertian Diffused Maxima Region. The unique and novel feature of this system is that it views the patients from both front and back and creates a 3D structure of the whole torso. By observing the 3D structure of the torso over time, the amount of air inhaled and exhaled can be estimated.

# Acknowledgements

This research project would not have been possible without the support of many people. Foremost, I would like to express my gratitude to my director of studies Dr. Lyndon Smith for his support and thoughtful guidance during my Ph.D study. In addition, I would like to acknowledge my supervisory team Professor Melvyn Smith, Dr. Jiulai Sun for their invaluable assistance in the completion of this thesis and for providing constructive feedback on my research throughout.

I am also thankful to all the participants who agreed to take part in this research study.

Finally, I would like to express my deepest gratitude to my family: mother, father, my brothers and sisters, my wife and my daughter for their endless patience, support and encouragement when it was most required.

***This work is dedicated to my family, especially Ami and Abu.***

# Contents

<b>1</b>	<b>Introduction</b>	<b>1</b>
<b>2</b>	<b>Pulmonary functional testing: State-of-the-art</b>	<b>11</b>
2.1	Contact based pulmonary functional testing . . . . .	12
2.2	Non-contact State-of-the-art Pulmonary Functional Testing . . . . .	17
2.3	Contact vs Non-Contact . . . . .	30
2.4	Conclusion . . . . .	33
<b>3</b>	<b>Photometric Stereo Based Pulmonary Functional Testing</b>	<b>35</b>
3.1	Photometric Stereo . . . . .	36
3.1.1	Assumptions and Limitation . . . . .	38
3.1.1.1	Multi-Spectral Photometric Stereo . . . . .	39
3.1.1.2	Shadows and Highlights . . . . .	40
3.1.1.3	Object Reflectance . . . . .	42

3.1.1.4	Object Motion . . . . .	50
3.1.1.5	Light Source Direction . . . . .	51
3.2	Photometric Stereo Setup and Data Acquisition . . . . .	52
3.3	Volume calculation from photometric stereo . . . . .	58
3.4	Conclusion . . . . .	60
<b>4</b>	<b>An Improved Photometric Stereo Through Distance Estimation And Light Vector Optimization From Diffused Maxima Region</b>	<b>62</b>
4.1	Introduction . . . . .	63
4.2	Background and related work . . . . .	65
4.3	Proposed Method . . . . .	67
4.3.1	Light source position estimation . . . . .	68
4.3.2	Object Distance Estimation . . . . .	73
4.3.3	Per pixel light direction calculation . . . . .	77
4.4	Experiments . . . . .	80
4.5	Results . . . . .	82
4.6	Conclusion . . . . .	89
<b>5</b>	<b>Non-Contact Pulmonary Functional Testing through an improved Pho- tometric Stereo Approach</b>	<b>90</b>
5.1	Calculating Absolute Amount of Air Volume . . . . .	91

5.1.1	Gradient to digital flow . . . . .	92
5.1.2	Digital flow to absolute volume . . . . .	93
5.2	Results . . . . .	96
5.3	Conclusion . . . . .	104
<b>6</b>	<b>Conclusions, Limitations and Future Work</b>	<b>106</b>
	<b>References</b>	<b>112</b>

# List of Figures

1.1	The most common parameters obtained using the Spirometer are visually demonstrated on the breathing wave. . . . .	4
2.1	A typical Pneumotachograph based pulmonary functional testing equipment . . . . .	13
2.2	A simple and common thermistor apparatus. . . . .	14
2.3	Typical construction of turbine based apparatus. . . . .	15
2.4	A typical ultrasonic based spirometer. . . . .	16
2.5	OEP: Markers Placement . . . . .	18
2.6	OEP: Full three-dimensional shape of the truck . . . . .	19
2.7	SLP projected pattern and corner detection . . . . .	20
2.8	SLP volume calculation . . . . .	21
2.9	SLP volume correlation . . . . .	22
2.10	Aoki <i>et al.</i> experimental setup . . . . .	23

2.11 Time-of-Flight based planes extraction . . . . .	24
2.12 Correlation of plane extraction between ToF and ANZAI belt AZ-733V	25
2.13 Time-of-Flight based obstructive sleep apnea monitoring . . . . .	26
2.14 AlignRT breathing monitoring system by Vision RT UK. . . . .	26
2.15 AlignRT clinical setup . . . . .	27
2.16 x during inhalation and exhalation . . . . .	29
2.17 Voscopoulos <i>et al.</i> contact based system. . . . .	30
3.1 Arrangement of incident, viewing, halfway and reflection vector. . .	43
3.2 Photometric stereo rig with subject standing in middle of rig . . . .	53
3.3 Block diagram of Hardware. Dotted arrows represent flow of camera trigger and light source power flow. Solid arrows represent flow of raw images and signal obtained from Pneumotachometer. . . .	54
3.4 Pneumotachometer volume (PV) signal obtained after digitization. Horizontal axis is time in seconds. Vertical scale is a normalized unit less representation of volume, to compare volume obtained from Pneumotachometer and Gradient. . . . .	55

3.5	Raw Images obtained from Front Rig. Image(a) when top-right light is turned on, image(b) when bottom-right light is turned on, image(c) when bottom-left light is turned on, image(d) when top-left light is turned on and image(e) is when no light is turned on. . . . .	57
3.6	Volume obtained from surface gradient (GV). Horizontal axis is time in seconds. Vertical scale is a normalized representation of volume, to compare volume obtained from Pneumotachometer and Gradient. . . . .	59
3.7	Comparison of Pneumotachometer Volume (PV) and Gradient Volume (GV) (combined front and back). Horizontal axis is time in seconds. Vertical scale is a normalized representation of volume. . . . .	60
4.1	Calibration setup for light position calculation and initial (Pseudo) light vector calculation. . . . .	70
4.2	(a) and (b) dot product of image with its light vectors. Diffused maxima regions are highlighted in dark red colour. (c) and (d) Diffused Maxima Regions centres are plotted on Height Map . . . . .	75
4.3	(a) Depth calculation using DMR and intersection of vector $O_v$ and $L^1$ . (b) Light vector calculation on each point of object surface. . . . .	76

4.4	(a) Image acquisition Setup. (b-f) images of Objects used in Experiments . . . . .	81
4.5	(a) Absolute Error in distance estimation from camera to object. (b) Mean angular error in surface normals. . . . .	83
4.6	(a) Integrated surface using traditional PS. (b) Integrated surface using Proposed method. (c) Surface scanned from 3dMD as a ground truth. . . . .	87
4.7	Slices of integrated surface . . . . .	88
5.1	Gradient Volume to Absolute volume conversion . . . . .	92
5.2	Pneumatic Apparatus . . . . .	95
5.3	Comparison of Pneumotachometer Volume (PV) and Gradient Volume (GV) (combined front and back). Horizontal axis is time in seconds. Vertical scale is a normalized representation of volume. . . . .	98
5.4	(a): front Gradient Volume (GV) and Pneumotachometer Volume (PV) plot, (b): back GV and PV plot. Horizontal axis is time in seconds. Vertical scale is a normalized representation of volume. . . . .	100

5.5	Subject displacement chart in Sagittal and Coronal plane. Vertical axis is the correlation between Gradient volume and Pneumotachometer volume. Horizontal axis is the displacement of subject from centre of rig in Sagittal and Coronal plane in centimeters. . . . .	102
5.6	(a) the plot of Pneumotachometer volume and Gradient volume in digital scale. (b) the plot of Pneumotachometer Volume and Gradient absolute volume in litres . . . . .	103

# List of Tables

4.1	Pseudo code of proposed method. . . . .	69
4.2	Tilt and Slant Light angle range for traditional PS and proposed method . . . . .	79
4.3	Mean Error . . . . .	85
5.1	Mean Angular Error in surface normal obtained using Photometric Stereo and 3dMD . . . . .	97
5.2	Gradient Volume analysis and comparison of front, back and com- bined GV . . . . .	99
5.3	Pseudo code of proposed method. . . . .	104

# List of publications arising from this work

## Journals

1. Jahanzeb Ahmad, Jiulai Sun, Lyndon Smith, Melvyn Smith, "Non-Contact Pulmonary Functional Testing through an improved Photometric Stereo Approach", [Submitted]
2. Jahanzeb Ahmad, Jiulai Sun, Lyndon Smith, Melvyn Smith, "An improved photometric stereo through distance estimation and light vector optimization from diffused maxima region", Pattern Recognition Letters, Special Issue on Depth Image Analysis. <http://dx.doi.org/10.1016/j.patrec.2013.09.005>

## Conferences

1. Jahanzeb Ahmad, Jiulai Sun, Lyndon Smith, Melvyn Smith, "Non-Contact Pulmonary Functional Testing through an improved Photometric Stereo Approach", MIUA 2014.
2. Jahanzeb Ahmad, Jiulai Sun, Lyndon Smith, Melvyn Smith, "Improving photometric stereo through per-pixel light vector calculation", BMVC Student Workshop, 13 September 2013, Bristol, UK.
3. Jahanzeb Ahmad, Jiulai Sun, Lyndon Smith, Melvyn Smith, John Henderson,

Anirban Majumdar, "Novel Photometric Stereo Based Pulmonary Function Testing", 3rd international conference and exhibition on 3D Body Scanning Technologies, Lugano, Switzerland, 16-17 October, 2012.

## **Abstracts**

1. Jahanzeb Ahmad, Jiuai Sun, Lyndon Smith, Melvyn Smith, "An improved photometric stereo through distance estimation and light vector optimization from diffused maxima region", BVI Young Researcher Colloquium, 25 June 2013, Cardiff, UK.
2. Jahanzeb Ahmad, "Novel Photometric Stereo Based Pulmonary Function Testing", Faculty of Environment and Technology, Doctoral Exchange, University of the West of England, 2 July , 2012, Bristol, UK,
3. Jahanzeb Ahmad, "An innovative hybrid 3D imaging system for tissue surface analysis", BMVA/EPSRC Computer Vision Summer School 27 June - 1 July 2011, Manchester, UK.
4. Jahanzeb Ahmad, "An innovative hybrid 3D imaging system for tissue surface analysis", BVI Young Researcher Colloquium, 30 June 2011, Bristol, UK.

5. Jahanzeb Ahmad, "An innovative hybrid 3D imaging system for quantitative surface analysis during surgery", Faculty of Environment and Technology, Postgraduate Research Student Conference, University of the West of England, 20 June, 2011, Bristol, UK.

# **Chapter 1**

## **Introduction**

Pulmonary functional testing is a series of tests used to determine the functionality of lungs. These tests calculate the amount of air inhaled and exhaled by the patient, the duration of inhalation and exhalation and how well the oxygen is delivered to the blood. The calculations help the health supervisor to determine whether the patient has a lung disease and/or how far along are they in the recovering process.

The test is commonly performed on patients suffering from certain types of lung diseases like shortness of breath, asthma, emphysema or pneumonia. It is also performed before and after a surgery or after giving certain medicine to see the effects on lung functionality.

The most commonly used technique for pulmonary functional testing is "Spirometry". It is attached to an instrument called "Spirometer" which records the amount and rate of air that is breathed in certain period of time. The test requires a patient to breathe in and out in a hand held mouth piece while in a sitting position. The patient has to breathe normally and quietly at some times, while at other times forced inhalation and exhalation after a deep breath is required. The results might differ in a standing position. The main issue with this test is that it has to be performed at the same position. Different positions might produce different results.

The measurements that can be obtained using a spirometer depend on the equipment used, but the most common and important measurements are defined below. Figure 1.1 gives a visual representation of these parameters.

### **Vital Capacity (VC)**

It is the maximum amount of air a person can exhale after inhaling the maximum amount of air. It is equal to the sum of inspiration reserve volume (IRV), expiratory reserve volume (ERV) and tidal breath. Vital capacity can be combined with other physiological measurements for diagnosis of underlying lung diseases. It is measured in litres, the normal adult vital capacity is between 3 to 5 litres but it varies depending on age, gender, height, mass, and ethnicity.

### **Forced Vital Capacity (FVC)**

Forced Vital Capacity is the maximum amount of air a person can forcefully exhale. FVC is used for the diagnosis of chronic obstructive pulmonary disease (COPD) because COPD causes the air in the lungs to be exhaled at a slower rate and in a smaller amount compared to a normal healthy person.

### **Forced Expiratory Volume in X seconds (FEV<sub>x</sub>)**

Forced expiratory volume is the maximum amount of air a person can forcefully exhale in the first x seconds of exhaling. It depends on age, gender, height and weight as well as ethnicity. It is also used for the diagnosis of COPD.

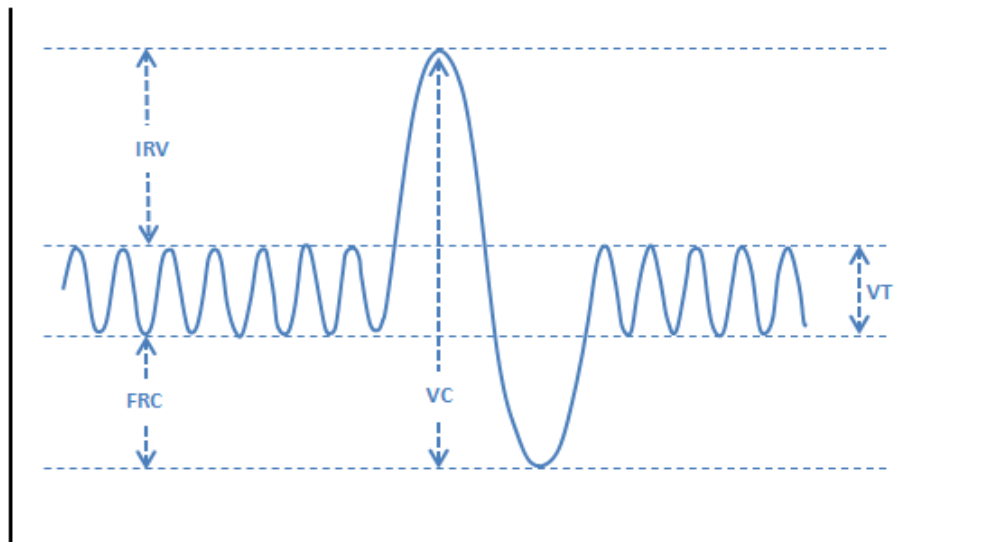


Figure 1.1: The most common parameters obtained using the Spirometer are visually demonstrated on the breathing wave.

### **Tidal volume (VT)**

It is the volume of air inhaled or exhaled in single breath in a rest position when extra effort is not applied. In a healthy, young adult, tidal volume is approximately 500 ml per inspiration or 7 ml/kg of body mass.

## **Motivation and Background**

Spirometry is the most common pulmonary function test, and that has been used by the clinicians and doctors for many decades. The patient has to hold a mouth piece and inhale and exhale into it. This contact based nature of the test brings about a few challenges and problems which need improvement.

Although spirometry involves minimal risks of any kind, there are however,

some restrictions. The test cannot be performed on patients having certain types of lung diseases. It is also not recommended for a person who recently had a heart attack, has certain other types of heart disease, or has had a recent collapsed lung.

Moreover, the results obtained by spirometry are highly dependent upon the patient's co-operation. Some of the main undesirable features of contact based spirometers are:

- Frequent calibration checks are needed throughout the lifetime of the device.
- Hygienic problems can be caused by the moisture and human secretions.
- Composition of air can affect the results of the Spirometer.
- The contact based nature and high degree of compliance requirement of the device makes it impossible to perform pulmonary functional testing on young, elderly and unconscious patients.
- Low flows are difficult to measure.

Research has also shown that the increased breath awareness may cause hyperventilation and alter the breathing pattern due to its contact based nature.

## **Aims and Objectives**

The main aim of this research was to develop a contact-less approach to perform the pulmonary functional testing by using photometric stereo method. Photometric Stereo provides high resolution 3D surface normals but it does not provide absolute dimensions of the object so a method was required to acquire this information without engaging any other imaging technique.

## **Contributions and Novelties**

The major contributions and novelties presented in this thesis are:

- Extending the practicality of photometric stereo especially for measurement and metrology tasks.
- The general assumption of a collimated light source in photometric stereo imaging setup is relaxed.
- Low frequency geometric distortion and systematic error due to imperfection in illumination direction is reduced.
- A novel method of estimating the distance of the object from the camera is developed without the need to use any additional imaging device. This is

achieved by employing diffused maxima regions on the object surface.

- Per-pixel light vector direction is calculated using distance estimation from Diffused Maxima Regions.
- Absolute dimensions of the object can be subsequently estimated from distance estimation.
- Per-pixel light vector calculation is dynamic so change in shape is compensated for every frame.
- When compared with traditional photometric stereo, the proposed method reduces the mean angular and height error so that it is low, constant and independent of the position of the object placement within a normal working range.
- Up to 45% improvement in surface normal error is achieved in synthetic as well as real data.
- Mean height error in the reconstructed surface is reduced up to 6 mm.
- One of the unique and novel features of the system is that it views the patients from both front and back and uses the whole torso to calculate the air volume.

- A correlation of 0.98 between relative breathing volume calculated from Photometric Stereo and Spirometer data is observed.
- Using diffused maxima region the relative amount of air volume is converted into the absolute amount of air. Correlation of up to 0.96 between absolute breathing volume calculated from Photometric Stereo and Spirometer data is observed.
- A novel non-contact approach is proposed and a device was designed to perform pulmonary functional testing on patients of any age.
- A unique feature of the device is that it needs very little calibration and no registration between front and back view, and generates 3D data at pixel-level.

## **Thesis Outline**

This chapter gives an overview of Pulmonary Functional Testing and Spirometry. Later it discusses the drawbacks of using this contact based method leading to the motivation of developing the new photometric stereo based technique for pulmonary functional testing.

Chapter 2 explains the contact and non-contact based systems and their com-

parison in detail. The aim of this chapter is to identify and understand non-contact pulmonary functional testing systems and their functionality. These systems are studied in detail and some of the related issues are discussed.

In chapter 3 the photometric stereo technique is introduced. An initial comparison of data obtained from photometric stereo and contact based traditional Spirometry is made to check the feasibility of the photometric stereo for the proposed task. It also discusses in detail the software and hardware development for data acquisition. In addition, calibration of the camera sensor and lens is discussed.

Chapter 4 discusses the methods to improve the surface normal accuracy. This accuracy is achieved by relaxing the assumption of collimated light sources, because in a real imaging set-up, collimated light sources are not possible. The chapter first discusses the distance calculation from photometric stereo followed by per-pixel light vector calculation. The practicality and accuracy of this method is also discussed towards the end of the chapter.

In chapter 5 the volume obtained from photometric stereo is correlated with volume obtained from a traditional Spirometer (ground truth). The volume obtained from photometric stereo is not in absolute scale so an additional calibration step is performed to convert it to absolute volume.

In the last chapter the conclusion is discussed and possible future work is presented.

## **Chapter 2**

### **Pulmonary functional testing:**

### **State-of-the-art**

In the last chapter an introduction to pulmonary functional testing was presented along with the potential issues related to the contact based nature of the device. This chapter first discusses the contact-based pulmonary functional testing devices, followed by more recent non-contact devices and systems built for pulmonary functional testing. The chapter is then concluded with discussions of the problems and issues related to contact based devices and how these issues can be resolved by a non-contact device.

## **2.1 Contact based pulmonary functional testing**

The most common devices used to perform Spirometry are flow-sensors, these are compact and portable. The flow of air inhaled and exhaled is measured, which is used to calculate the volume of the air. This subsequent calculation is performed usually using a microprocessor. One of the biggest challenges in developing these devices is the calibration process to accurately detecting a low flow of air. These devices also need periodic calibrations to make sure that they are giving correct output [65].

There are four [78] main types of flow sensing devices:

1. Pneumotachograph

2. Thermistor

3. Turbine

4. Ultrasonic

## Pneumotachograph

Pneumotachograph uses differential pressure to estimate flow of the air. It is composed of a mesh which creates an air resistance, this resistance creates pressure difference. This differential pressure is measured with the help of a transducer and a computer or microprocessor. Figure 2.1 shows the typical construction of a Pneumotachograph.

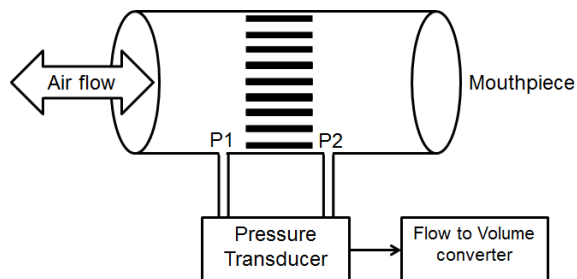


Figure 2.1: A typical Pneumotachograph based pulmonary functional testing equipment

## Thermistor

Thermistor or Hot-Wire anemometer consists of a tube with a heated wire. An electric current source is used to heat the wire at a particular temperature. As air passes through this tube, the temperature of the wire drops and additional current is needed to maintain the temperature of the wire. This additional current is converted into the flow of the air, after doing calibration. Some manufacturers have introduced a second heated-wire, to increase the accuracy of the measurement. One of the major problems with this device is that the hot-wire is very fragile and is also sensitive to movement of the apparatus during test. A simple and common apparatus is shown in figure 2.2.

Modern thermistor flow sensing devices are also called mass flow-meters. Mass flow-meters are able to measure the amount of gas molecules as they pass through the tube. This makes it more accurate, as it is not influenced by the temperature and viscosity of the air.

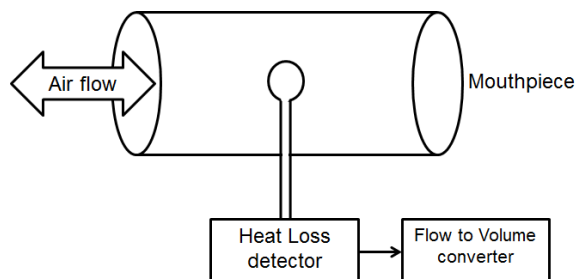


Figure 2.2: A simple and common thermistor apparatus.

## Turbine

This device measures the flow of the air by using the principle of a turbine in which a wheel rotates as air passes through the tube. A light emitting diode (LED) and a photo-sensor are placed in the turbine, where rotation of the wheel blocks the light from the LED, to the photo-sensor. This creates impulses of the light that are proportional to the flow of the air. After calibration, the frequency of the impulses can be translated to the flow of the air and total count of the impulses to the volume of the air. One of the main challenges in development of this device is the weight of the turbine wheel. It should be as small as possible to avoid any errors in measurements due to inertia of the wheel. Figure 2.3 shows the typical construction of turbine based apparatus.

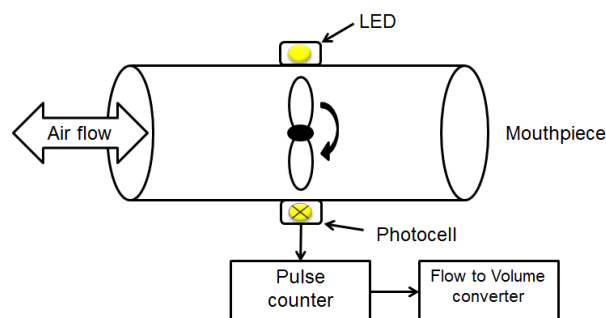


Figure 2.3: Typical construction of turbine based apparatus.

## Ultrasonic

Ultrasonic devices use the principle of time-of-flight to measure the flow of the air through a tube. Two ultrasound elements are placed in the sensor housing and alternating pulses are emitted in both directions. Depending on the direction and velocity of air flow, the time of the flight of the pulses changes. This change in the time of the flight is proportional to the flow of gases but is independent of the gas temperature, viscosity or humidity of the gases, which makes it more accurate as compared to the other three techniques. A typical ultrasonic based spirometer is shown in figure 2.4.

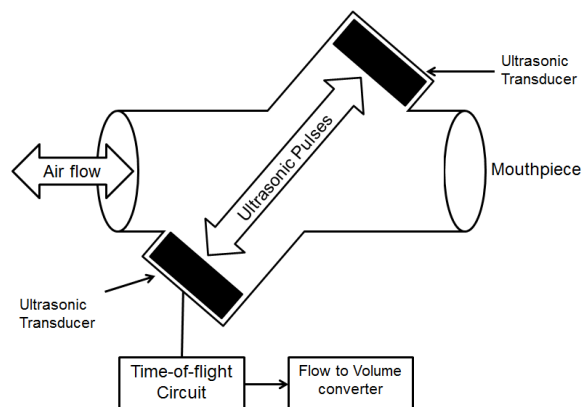


Figure 2.4: A typical ultrasonic based spirometer.

## **2.2 Non-contact State-of-the-art Pulmonary Functional Testing**

The main aim of this research is to develop a respiratory functional testing method using a non-contact vision based method, thus in this section vision based pulmonary functional testing methods and systems are discussed. Non-contact vision based respiratory monitoring systems are also discussed.

### **Optoelectronic Plethysmography System**

Optoelectronic Plethysmography System was the first optical system for pulmonary functional testing. The pioneering work was done by Giancarlo and Antonio [30] in 1985 and the system was called The ELITE (ELITE System; BTS, Milan, Italy). They used a digital video system and motion analyzer system to identify and track predefined markers already placed on person's torso. By tracking the markers they were able to construct a 3D model of the respiratory ribcage and abdomen. By monitoring the expansion and the contraction of this 3D model they were able to quantify the change in volume which corresponds to measurement of breathing. The main problem with this system was its higher error (21.3%), when compared with a traditional Spirometer [20]. The error was caused by the

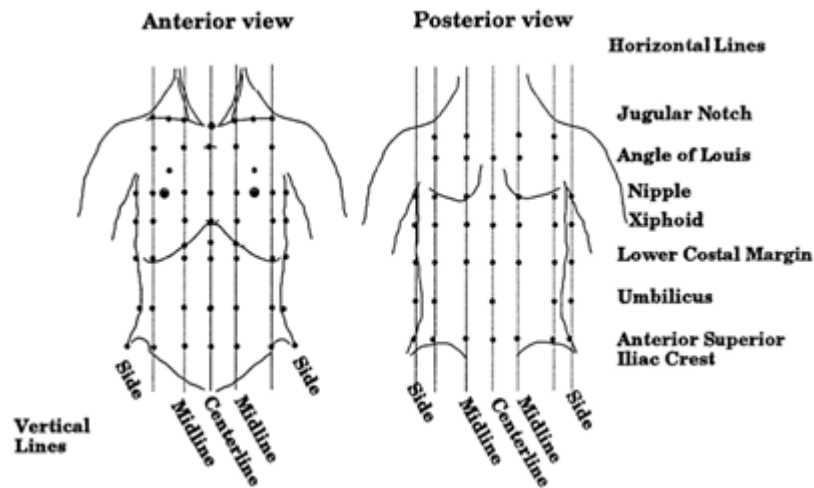


Figure 2.5: OEP: Markers Placement

assumption of a cubical geometry of chest wall shape.

Later many researchers modified this assumption to circumferential geometry to improve the accuracy of measurement [6, 19, 20]. The 86 markers method used by Cala *et al.* in 1996 [20] reduced the error of ELITE to less than 3.5%. Placements of these markers are shown in Figure 2.5. Cala also patented his method and renamed it to OptoElectronic Plethysmography system (OEP) (OEP System; BTS, Milan, Italy). The OEP measures the volume in three different regions of the chest and the abdomen by tracking markers with up to eight cameras (four for front and four for back). A full three-dimensional shape of the torso is constructed (Figure 2.6) and the volume is calculated using Divergence Theorem [80], also known as Gauss's theorem.

Cala *et al.* showed that there is a strong correlation between volume measured from the OEP and volume measured from the Spirometer [20] both in quiet

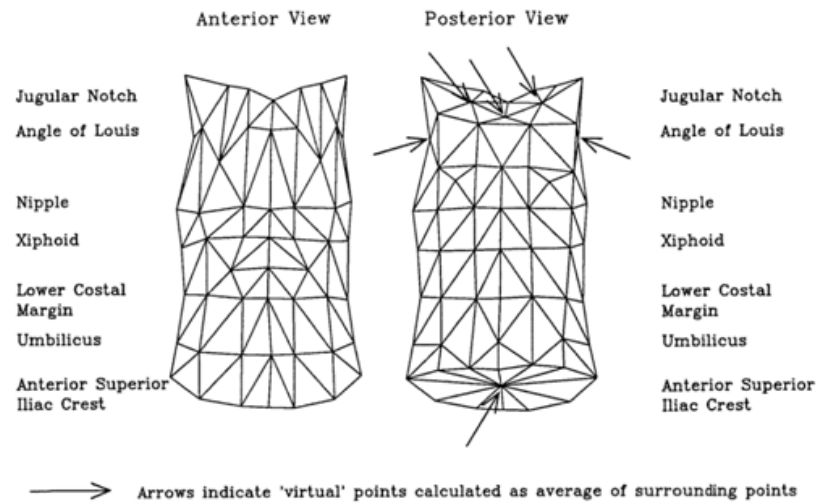


Figure 2.6: OEP: Full three-dimensional shape of the truck

breathing as well as in different vital capacity manoeuvres. OEP has been also validated for variety of conditions like intensive care patients [5], in infants [25] and during exercise in chronic obstructive pulmonary disease [6, 7, 33]. It has been also validated on subjects with prone and supine positions [4]. Although the concept of vision based Spirometry is validated, this system is not a non-contact system as this needs marker placed on human torso.

## Structured Light Plethysmography (SLP)

Recently a group of researchers from Cambridge University, Cambridge UK and PneumaCare Limited, Duxford UK have developed a new Non-Contact (marker-less) system for respiratory functional testing [23]. They use structured light method [84] to capture three-dimensional data from a patient's chest by using two digital camera and a projector. Both cameras have been placed in different



Figure 2.7: SLP projected pattern and corner detection

but known positions and angles with respect to patient's chest. The patient is requested to wear a tightly fit white T-shirt and then to sit on a firm back chair or lay down on a mat in the supine position. After placing the rig in appropriate position the patient is asked to breath in a natural way. They use the Sobel edge detector to locate the corners of the projected pattern as shown in Figure 2.7.

The corners are tracked and corresponded with images from both cameras to construct the three-dimensional shape of the scene. After removing unwanted data and filling the missing data points, only the chest's three-dimensional shape is remaining. The volume of the given chest's three-dimensional shape is calculated between the chest and the back of the chair or mat as shown in Figure 2.8. Like OEP they also used Gauss's Theorem [80] for volume calculation. The validation of the system was performed on 40 healthy subjects, a strong correlation with Spirometer data was found and is shown in Figure 2.9. However the system still needs further validation on real patients and the trail is in progress at Addenbrookes NHS Hospital, Cambridge UK. The current system features low spatial

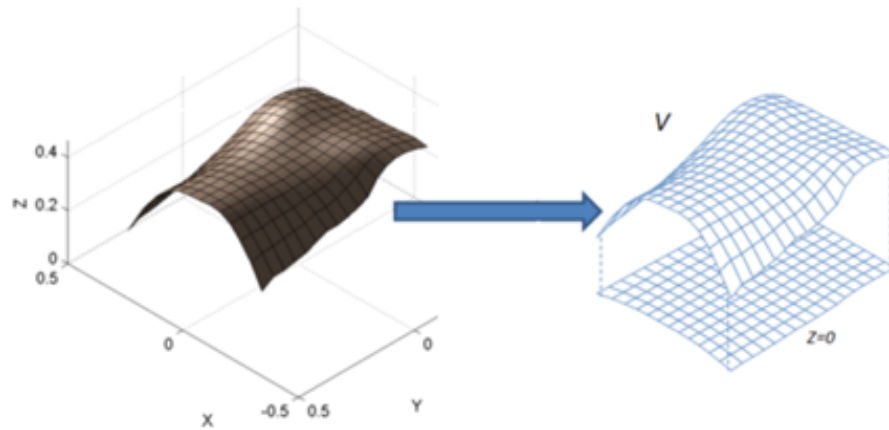


Figure 2.8: SLP volume calculation

and temporal resolution and cannot handle changes in physical movement of the patient.

## Laser based Systems

In 1997 Kondo *et al.* [50] developed a single laser line based commercially available system to monitor chest wall movements. They performed three different kinds of tests, two using lung models and one using healthy adults. Although they have found a strong correlation between laser line and Spirometer data, using only one laser line does not enable capture of any differences between volume due to right or left lung.

In 2011 Tsujimura and Nakamura [73] evaluated the fiber-grating (FG) vision sensor for assessing pulmonary functional testing. They measured tidal volume on five subjects as a control unit and found correlation of 0.98 between the

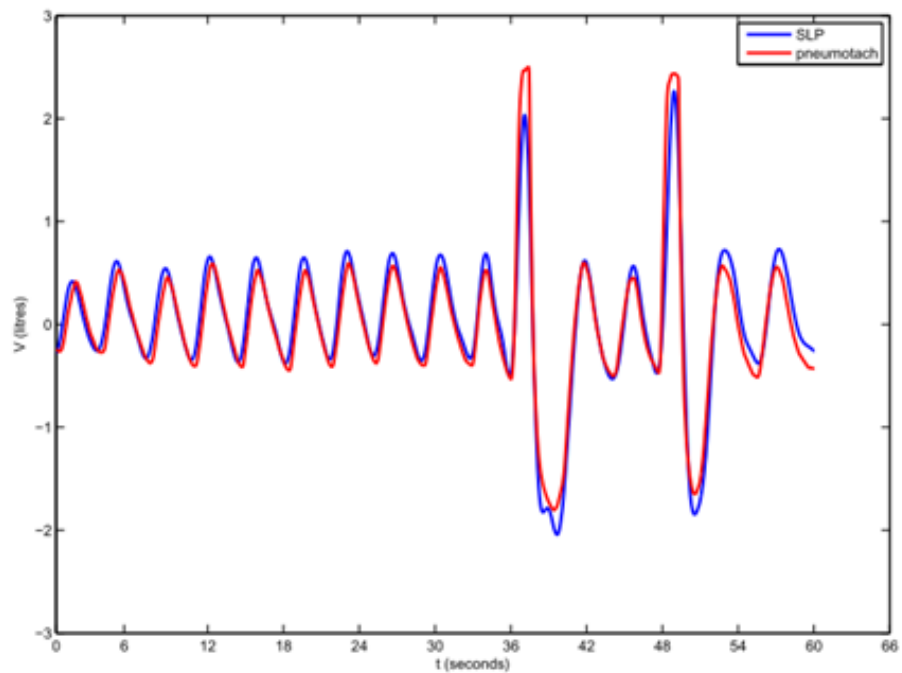


Figure 2.9: SLP volume correlation

Spirometer and the FG system. They also performed tests on COPD patients and found that FG is capable of measuring volume changes to be used for pulmonary functional testing.

Aoki *et al.* [9] in 2005 presented a triangulation based respiration monitoring and measurement method. The system was based on fibre grating vision sensors, which is composed of multiple slit light projector and CCD camera. It projected 300 bright spots on the sleeping patients. These projected points are then observed from a CCD camera and processed on data processor to generate 3D data (Figure 2.10). This system can capture and calculate volume up to 5 frames per second using a triangulation method. Validation was performed by simultaneously measuring volume from a 3D data and a Spirometer, the mea-

Redacted due to copyright



Figure 2.10: Aoki *et al.* experimental setup

Measurements from these two devices showed a high correlation of 0.96. In spite of high correlation the system has very low spatial and temporal resolution.

## Respiratory Monitoring Systems

Respiratory motion can be very easily detected using Time-of-Flight(ToF) technology. Jochen Penne and *et al.* in 2008 [62] proposed a ToF based system capable of providing a one-dimensional breathing signal for respiratory gauging. A ToF camera was mounted on a rigid surface 60-100 cm away from the patient. Firstly an empty table is calibrated and marked as plane 1 as shown in Figure 2.11. Once the patient is lying on the table, the torso is segmented by removing all the points which are away from the table-plane. After that two regions of interest are defined, one for the abdomen and one for the chest.

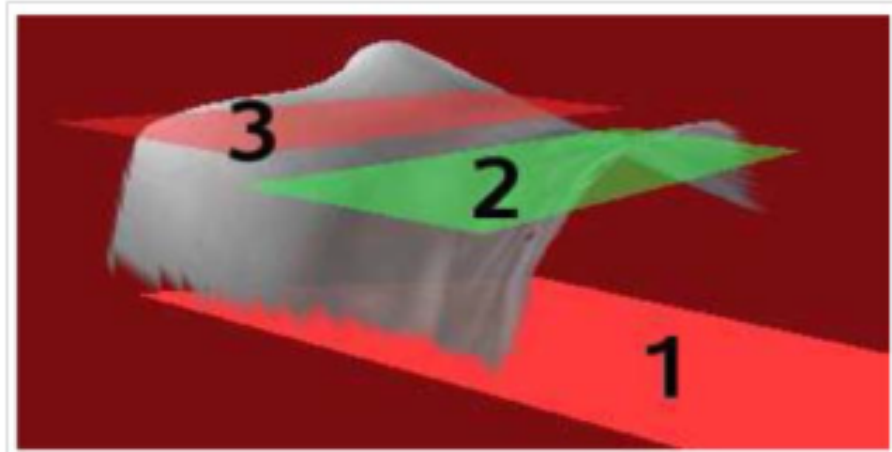


Figure 2.11: Time-of-Flight based planes extraction

The noise from ToF data is removed by using a mean filter with filter size of five; subsequently a plane is fitted to this segmented data using least-square fitting. Both planes were forced to be parallel with the initial table plane 1 yielding plane 2 and plane 3 as shown in Figure 2.11. Plane 3 represents the motion of the chest and plane 2 represents the motion of the abdomen. For validation they correlated the computed breath signal from ToF with the breath signal from ANZAI belt AZ-733V [53]. The system was tested on 13 patients and the results of the correlation are summarized in Figure 2.12.

Their average correlation is 0.85 for thoracic respiration and 0.91 for abdominal respiration. They have also claimed that the low correlation is due to bad respiration signals delivered by the ANZAI belt. Regardless of low correlation, the assumption that the breathing movement is only in one-dimension is not appropriate. Especially in scoliosis the deformation of the torso is very complex so a

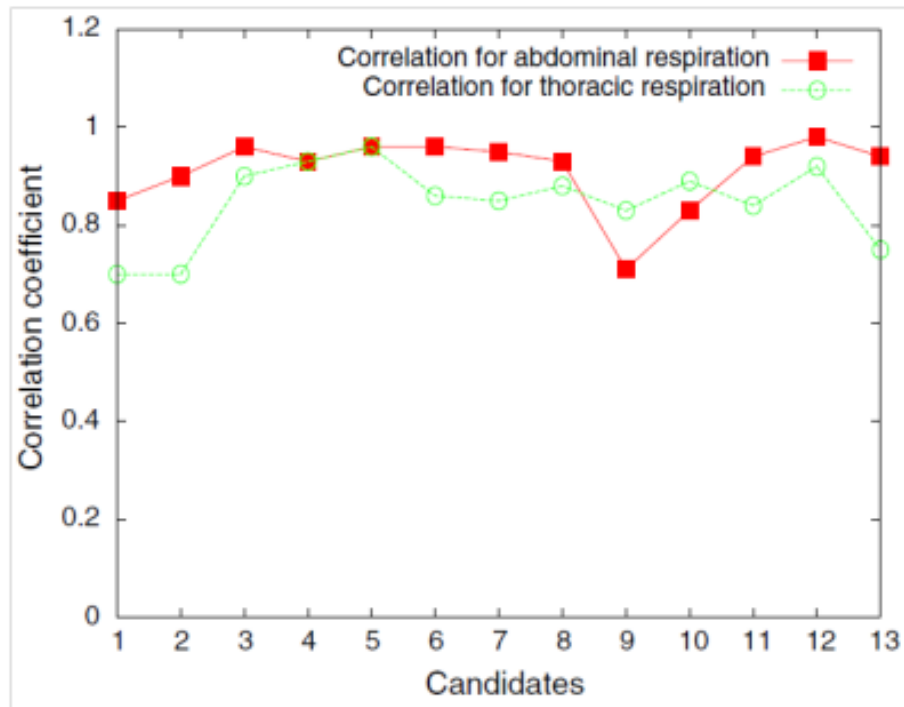


Figure 2.12: Correlation of plane extraction between ToF and ANZAI belt AZ-733V movement only based method cannot produce a meaningful result.

In 2009 Kerstin Muller *et al.* [61] used the same system developed by Jochen Penne *et al.* for automatic classification of breathing into two classes i.e. chest and abdominal breathing; however the system is not properly validated. In 2010 Falie and Ichim [28] also used ToF for respiratory monitoring. They divided the image into 12 different sections (Figure 2.13) and then observed the movement in these sections. By observing these movements they claimed to have detected sleep Apnea. However the system is not validated properly as it assumes that the patient is lying straight and facing towards the camera.

Vision RT is a UK based company which has developed a respiratory monitoring system for radiotherapy called AlignRT [55]. AlignRT utilises two or three

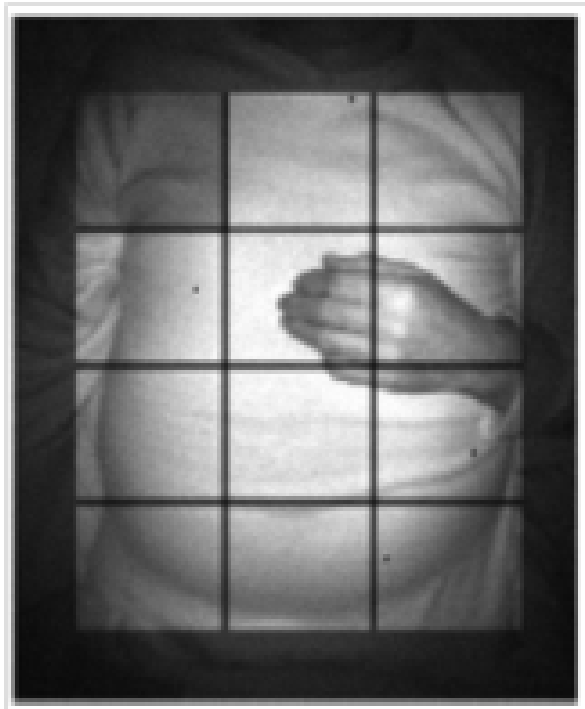


Figure 2.13: Time-of-Flight based obstructive sleep apnea monitoring



Figure 2.14: AlignRT breathing monitoring system by Vision RT UK.

ceiling mounted, marker-less stereo vision camera units, a single unit is shown in Figure 2.14. The system is first calibrated using a known size object before use. The 3D surface model of the patient is computed by doing correspondence between each data point from data camera. The 3D surface data from multiple units is combined to produce a complete model which extends all the way around the patient.

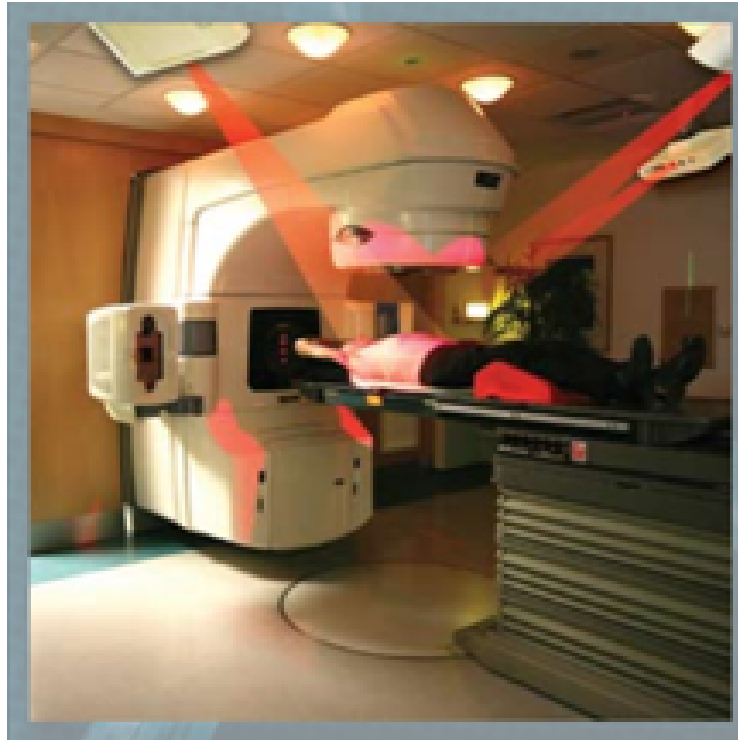


Figure 2.15: AlignRT clinical setup

AlignRT is a well established technology and is being used in many clinical setups. A typical AlignRT clinical setup with three AlignRT units is shown in Figure 2.15. It is currently being used for Breast Treatment, Intracranial Stereotactic Radiotherapy, Sarcomas, General Patient positioning as well as Surveillance [55]. AlignRT is also clinically tested, validated and has been published [17, 34, 45, 59, 64, 75].

Aoki *et al.* [10] reported a non-contact visual sensing method to detect the respiration pattern by using a fiber grating (FG) vision sensor and processor unit. Their system consisted of FG projecting device which provided an array of invisible infra-red light spots and a CCD camera with an optical band-pass filter. The

moving distances of bright spots projected from projector was captured by CCD camera where each image was analysed to monitor respiration.

Tan *et al.* [72] in 2010 proposed a video camera and desktop based system for respiratory rate monitoring. Each recorded image in a video sequence has a time stamp  $t$ , the difference between image at time  $t$  and  $t_d$  was calculated, where  $t_d$  represents the time few frames before  $t$ . An increase in the value of  $t_d$  caused faster algorithm operation, but decreased the resolution of the algorithm in detecting movements. In this study a value of 0.5 sec was used for  $t_d$  as it was observed to provide an acceptable compromise between the resolution and speed. The difference image was then converted to binary image by applying thresholding. The sum of pixel values in the binary image represented the movement between  $t$  and  $t_d$ . These values were represented as  $x(t)$  and then plotted against time to obtain a respiration signal. A plot of these values during exhalation and inhalation is provided in Figure 2.16. The vertical axis of the plot represents chest and abdominal movements. During exhalation, the chest wall initially moves slowly inward, its movement increases with time, reaching a peak and then the amount of movement decreases. A similar process occurs during inhalation, but this time the chest wall moves outward. An algorithm was developed to extract the respiration rate from the recorded signal in real-time.

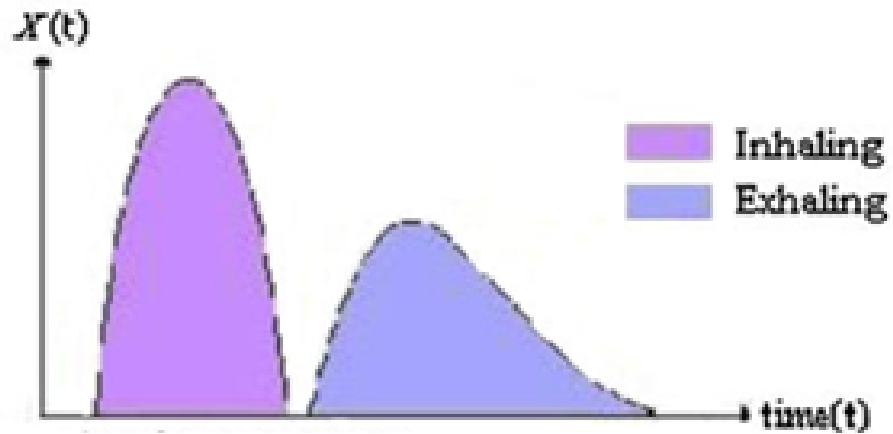


Figure 2.16:  $x$  during inhalation and exhalation

Recently in 2012 Povsis *et al.* [63] developed a laser pattern based system which observes the laser pattern distortion from multiple views and uses that to generate 3D data. The main aim of this system was to teach breathing exercises. The subject was observed from both front and back at the same time with different wave-length lasers and filters. Although the shape measurement accuracy is quite high ( $\pm 0.7\text{mm}$ ) the spatial resolution of the technique is limited to spacing between laser lines and size of the laser lines. Safety might also be an important issue with the use of a laser.

Recently Voscopoulos *et al.* [77] in 2013 developed a non-invasive but contact-based system (shown in Figure 2.17) to measure the tidal volume and respiratory rate. Their primary study was based on thirty one subjects. They found less than 10% average error between their system and traditional Spirometer.

Redacted due to copyright



Figure 2.17: Voscopoulos *et al.* contact based system.

## 2.3 Contact vs Non-Contact

Many researchers have compared contact based Spirometer methods with non-contact methods leading to a conclusion that the contact based nature of the Spirometer equipment creates hyperventilation and can alter the breathing pattern. There are also a few publications, which suggest that with non-contact system can achieve the same level of measurements as with a traditional spirometer.

Some of the outcomes are summarised in this section.

In 1972 Gilbert *et al.* [35] performed experiments on 6 healthy as well as 8 patients suffering from respiratory diseases. They used electromagnetic sensors to detect the changes in the anterior-posterior diameter of the chest and abdomen and used these changes to compute the tidal volume. They showed that it was

closely correlated with the tidal volume obtained from the Spirometer. They also found that there was an increase in the tidal volume when a mouthpiece based Spirometer was used. A decrease in respiratory frequency was also found and was believed to be due to the irritating effects of the nose-clip and mouthpiece. Similar experiments were also performed by Askanazi *et al.* [12, 13] in 1978 and 1980 on healthy subjects and patients showing that the use of a mask or mouthpiece and nose-clip alters the breathing pattern and vital capacity. Western and Patrick [81] in 1988 also performed similar experiments and found that face mask causes prolonged inspiration and increased tidal volume.

In 1995 Bloch *et al.* [18] extended the normal breathing experiments to observe the effects of mouthpiece breathing on the cardiorespiratory response during intense exercise. Experiments were performed on six normal men while recording ECG and breathing pattern with a respiratory inductive plethysmograph. Each participant performed exercises to volitional exhaustion twice, once with and once without mouthpiece and nose-clip. Experiments showed that breathing through mouthpiece increased tidal volume by 63% and respiratory rate by 33% during mild exercise. However they did not find any alteration in performance, heart rate, or breathing pattern at maximal exercise. They concluded that mouthpiece and nose-clip do not alter the breathing pattern and performance during

maximal exercise.

Han *et al.* [36] in 1997 performed three different kinds of experiments on 40 females and 34 males. Two of the experiments required the patients to use the mouthpiece, while the third type of experiment was performed without the mouth piece. In one of the experiments with a mouthpiece, the subject was led to believe that recording apparatus is being calibrated and data is not recorded. They found that awareness of data recording decreases breathing irregularities (sigh and end-expiratory pauses). It also caused prolongation of inspiratory and expiratory time. They also found that breathing through mouthpiece induced some respiratory discomfort particularly in females.

Bastianini *et al.* [15] in 2009 used a Opto-Electronic Plethysmograph (OEP) [4, 20] to show that it can be used as diagnosis device for asymmetric respiratory rehabilitation. They used tidal volume for respiratory rehabilitation efficacy. Tidal volume variation of six torso and chest regions were measured on pre and post surgery of 14 patients undergoing left or right superior lobectomy. 32% increase in mean tidal volume was observed for non-operated side between pre-surgery and post-surgery. The increase in tidal volume on the non-operated side suggests that OEP is suitable for respiratory measurement as an increase in tidal volume of one side is not detectable using mouthpiece based Spirometer.

In 2010 Fregadolli and Sasseron [31] did a comparison between breathing through a mouthpiece and a face mask. 60 healthy participants participated in the study; statistical analysis showed significant difference between the two methods which suggests that mouthpiece and face mask can change the breathing pattern.

Recently in 2013 Layton *et al.* [52] compared OEP system with Spirometer during maximal exercise. They found a very high correlation of vital capacity between Spirometry and OEP, they also found that the actual difference between the two measurements was insignificant. This high correlation and insignificant difference in both measurements suggests that non-contact PFT can be used, not only in the rest state but also during exercise.

## **2.4 Conclusion**

In this chapter contact based and non-contact based pulmonary functional testing systems were presented along with a review of the different experiments performed by researchers to compare both methods. Most of the researchers found that the contact based nature of the traditional Spirometer can cause increased breathing awareness which can subsequently cause inaccurate measurements.

In the next chapter initial experiments based on non-contact photometric stereo based device are presented. Also photometric stereo methods are discussed in

detail.

## **Chapter 3**

### **Photometric Stereo Based**

### **Pulmonary Functional Testing**

In this chapter, a photometric stereo based non-contact pulmonary functional testing setup is evaluated. The working principle of Photometric Stereo is explained along with the general assumptions and limitations of this method. In the middle part of the chapter the materials and methods used in development of the experimental setup are discussed. This is followed by the proposed method of calculating the volume information from the gradient information obtained from Photometric Stereo.

### **3.1 Photometric Stereo**

Photometric Stereo was first introduced by Woodham in 1980 [82]. It recovers the surface shape of the object or scene by taking several images from the same view point but under different lighting conditions. Multiple light sources are placed at different angles but at equal distance apart from the object. Each pixel at the same location within all the images is assumed to correspond to the same object point so there is no need to match features between images.

The main assumption of Photometric Stereo is that the object's surface is Lambertian and that the surface reflectance obeys Lambert's Law. According to the Lambertian reflectance model the intensity of light reflected from an object's surface is dependent on the surface albedo  $\rho$  and the cosine of the angle of the

incident light as described in Equation 3.1. The cosine of the incident angle can also be referred as dot product of the unit vector of the surface normal  $\vec{N}$  and the unit vector of light source direction  $\vec{L}$ , as shown in Equation 3.2.

$$I = \rho \cos(\phi_i) \quad (3.1)$$

$$I = \rho(\vec{L} \cdot \vec{N}) \quad (3.2)$$

When more than two images (four images are used in the following work) from the same view point are available under different lighting conditions, we have a linear set of Equation 3.1 and 3.2 and this can be represented in vector form as shown in Equation 3.3.

$$\vec{I}(x,y) = \rho(x,y)[L]\vec{N}(x,y) \quad (3.3)$$

$\vec{I}$  is the vector formed by the four pixels  $((I^1(x,y), I^2(x,y), I^3(x,y), I^4(x,y))^T$  from four images,  $[L]$  is the matrix composed by the light vectors  $(\vec{L}^1; \vec{L}^2; \vec{L}^3; \vec{L}^4)$ , where, 1, 2, 3 and 4 represents individual light source direction.  $[L]$  is not a square and so it is not invertible, but the least square method can be used to compute Pseudo-Inverse and the local surface gradients  $p(x,y)$  and  $q(x,y)$ , and

the local surface normal  $N(x,y)$  can be calculated from the Pseudo-Inverse using Equations 3.4,3.5 and 3.6 where  $\vec{M}(x,y) = (m_1(x,y), m_2(x,y), m_3(x,y))$ .

$$\vec{M}(x,y) = \rho(x,y)N(x,y) = ([L]^T [L])^{-1} [L]^T \vec{I}(x,y) \quad (3.4)$$

$$p(x,y) = \frac{-m_1(x,y)}{m_3(x,y)}, q(x,y) = \frac{-m_2(x,y)}{m_3(x,y)} \quad (3.5)$$

$$N(x,y) = \frac{[p(x,y), q(x,y), 1]}{\sqrt{p(x,y)^2 + q(x,y)^2 + 1}} \quad (3.6)$$

$$\rho(x,y) = \sqrt{m_1^2(x,y) + m_2^2(x,y) + m_3^2(x,y)} \quad (3.7)$$

### 3.1.1 Assumptions and Limitation

Photometric Stereo estimates the surface normals under the following main assumptions.

1. Images are Gray scale.
2. There are no shadows and specular highlights in images.
3. The surface of object obeys Lambertian reflectance.

4. Light direction is known.
5. Light source is at infinite distance.
6. Object is static during image capture.

#### **3.1.1.1 Multi-Spectral Photometric Stereo**

Photometric Stereo assumes that the images are captured using monochrome light sources and camera. However Multi-Spectral methods have been developed recently to get higher frame rates and less motion artefacts. In addition, by using colour cameras researchers have also tried to improve the accuracy of photometric stereo by utilizing the colour information.

Barsky and Petrou [14] employed a four source colour photometric stereo set-up and used spectral and directional cues to improve photometric stereo by detecting shadows and highlights.

Fyffe *et al.* [32] presented a method in 2011 based on two colour cameras by using a prism and filters. They were able to capture six different channel images from two single shots. Although they have not mentioned the accuracy or improvement in surface normals due to unique data acquisition set-up. However this method has potential to produce improved surface normals in moving objects.

Anderson *et al.* in 2011 [8] developed a complex procedure to capture the

dense normal map of a moving object. They used stereo low resolution geometry and object reflectance properties to capture high resolution and dense surface normals of moving objects.

Vogiatzis and Hernandez [76] used colour photometric stereo to capture the human face. The main challenge for multi-spectral photometric stereo is the calibration process. Multiple wavelength light sources can interact with each other due to subsurface scattering in human skin. This subsurface scattering results in human skin being non-Lambertian. By asking the subject to make a rigid motion Vogiatzis and Hernandez were able to create a coarse 3d model of the face. The coarse model was then used to estimate the lighting parameters and purely diffused points. The remaining points were then solved through non-linear optimization.

### **3.1.1.2 Shadows and Highlights**

Shadows and specular highlights in captured images can cause high degree of error in the surface normals and in the reconstructed surface. Highlights usually lead to an over determined surface and shadows usually lead to an under determined surface. One simple way to handle shadows and highlights is to capture more than three images with different light sources and to discard pixels in images

which represent shadow or highlight. But when only three images are available this problem becomes quite challenging.

Sun *et al.* [71] presented an efficient selection criteria in order to avoid specular highlights and shadows in six image photometric stereo.

Hernandez *et al.* [40, 41] presented a Markov Random Field (MRF) based optimization scheme, to segment shadow regions from photometric stereo images. They achieved this by assuming the surface to be integrable. By using this assumption a unique solution can be obtained for the shadow region. The scheme also showed that the method can be performed in a colour photometric stereo set-up where inter-reflection and shadows occur.

Recently in 2013 Mecca *et al.* [57, 58] presented a new Partial Differential Equation (PDE) based method. It estimates the reconstructed surface directly rather first computing the surface normals and then integrating them. This direct method also deals with shadows while computing the surface from captured images. According to the authors their method is numerically very stable and can handle very large images with fast processing time.

### 3.1.1.3 Object Reflectance

Several models exist that describe this complex interaction of light with different materials. These models can be categorised into theoretical, empirical and simulation based models. Some of these models can be used to describe the absorption and transmission characteristics of surfaces that are translucent while others are limited to opaque materials. The following sections will discuss different reflectance models and their particular features.

#### Lambertian Model

The Lambertian model is one of the simplest reflectance models. It describes the light interaction with a surface as ideal diffuse, meaning a surface appears equally bright from all viewing directions; hence making the model independent of the viewing direction. Most real world surfaces are not Lambertian; however due to its simplicity, this model is frequently used with photometric stereo to recover surface normals. According to this model the amount of reflected light from a surface is dependent on the angle between the surface normal  $\vec{n}$  and the light source direction  $\vec{I}$ .

$$L(\omega_i) = \frac{k_d}{\pi} E \cos \theta_i = \frac{k_d}{\pi} E (n \cdot l) \quad (3.8)$$

Where  $E$  is the intensity of light source or irradiance and  $k_d$  is the diffuse reflection coefficient. Division by  $\pi$  in the denominator is included for energy conservation. Real world surfaces cannot be accurately modelled by just using a Lambertian model particularly if they are glossy or shiny because the specular component is not accounted for.

The geometry of incident illumination  $\vec{L}$ , viewing direction  $\vec{V}$ , surface normal  $\vec{N}$ , reflection  $\vec{R}$  and Halfway vector  $\vec{H}$  will be used from now on in most of the reflectance models and is shown in Fig. 3.1.

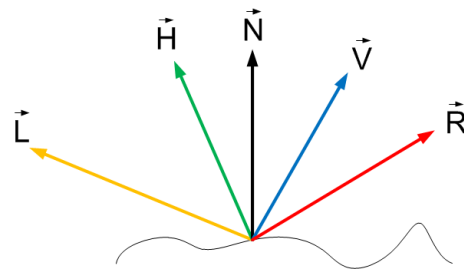


Figure 3.1: Arrangement of incident, viewing, halfway and reflection vector.

### Phong and Blinn-Phong Model

The Phong reflectance model (eq. 3.9) is composed of both a diffuse and a specular component. The specular fall off is determined by the angle  $\theta_s$  which

is the angle between  $\vec{\mathbf{R}}$  and  $\vec{\mathbf{V}}$ . The variable  $\alpha$  determines the size of the lobe, where a higher  $\alpha$  will result in sharp lobe while a lower value will produce a wide specular lobe.

$$L = (I_a + k_d(\cos \theta_i) + k_s(\cos \theta_s)^\alpha) \quad (3.9)$$

$I_a$  is the ambient term while  $k_d$  and  $k_s$  are the diffuse and specular reflection coefficients.

To make it more computationally efficient Blinn replaced the reflection vector with the Halfway vector defined by:

$$\vec{\mathbf{H}} = \frac{\vec{\mathbf{L}} + \vec{\mathbf{V}}}{|\vec{\mathbf{L}} + \vec{\mathbf{V}}|} \quad (3.10)$$

So the Blinn-Phong model is written as:

$$L = (I_a + k_d(\cos \theta_i) + k_s(\cos \theta_h)^\alpha) \quad (3.11)$$

$$L = I_a + k_d(\vec{\mathbf{L}} \cdot \vec{\mathbf{N}}) + k_s(\vec{\mathbf{N}} \cdot \vec{\mathbf{H}})^\alpha \quad (3.12)$$

In summary, all the components involved in Blinn and Blinn-Phong model are:

- $I_a$  is the ambient term.
- $k_d$  and  $k_s$  are the diffuse and specular reflection coefficients.
- $\vec{L}$  is the direction of a light source.
- $\vec{V}$  is the viewing vector.
- $\vec{H}$  is the unit Halfway vector.
- $\vec{N}$  is the surface normal.
- $\vec{R}$  is the vector for reflected light,
- $\alpha$  is the specular fall off and its value determines the size of the lobe.

### **Oren Nayer Model**

The Oren Nayer model provides a more realistic approach to rough surfaces by providing more reflected radiance for retroreflection (i.e. when the viewing direction approaches the direction of incidence). Most rough surfaces like clay, plastics exhibit increased reflected radiance at retroreflection angles which cannot be accurately modelled by a Lambertian model as the Lambertian model produces dark effects at occluding boundaries for rough surfaces. This model is based on the

microfacet theory in which the surface is considered to be made of of v-shaped cavities.

$$L_r = \frac{\phi}{\pi} \cdot \cos(\phi_i) \cdot (A + (B \cdot \max[0, \cos(\phi_i - \phi_r)]) \cdot \sin(\alpha) \cdot \tan(\beta)) \cdot E_0 \quad (3.13)$$

Where

$E_0$  is the irradiance when the facet is illuminated head-on.

$$A = 1 - \frac{1}{2} \frac{\sigma^2}{(\sigma^2 + 0.33)} \quad (3.14)$$

$$B = 0.45 \frac{\sigma^2}{\sigma^2 + 0.09} \quad (3.15)$$

$$\alpha = \max(\theta_i, \theta_o), \quad \beta = \min(\theta_i, \theta_o) \quad (3.16)$$

### **Torrance-Sparrow Model**

The Torrance and Sparrow model [22] is also a microfacet based model, however it differs from the Oren Nayer model by modelling each microfacet as a perfect reflector as opposed to a perfect diffuser. The modelling of a surface as a group of microfacets originates from the fields of optics and radiation transfer.

$$f_s = \rho_s * \frac{1}{\pi} * \frac{FDG}{(\vec{N} \cdot \vec{V})(\vec{N} \cdot L)} \quad (3.17)$$

where the term  $D$  determines the microfacet distribution . Each microfacet is considered to be perfectly specular.  $F$  is the Fresnel reflection, and the parameter  $G$  (Geometric attenuation factor) contributes the amount of light after masking and shadowing of the microfacets.

The Fresnel term describes the amount of light reflected due to the refraction index of the material at a particular incident angle. The Fresnel equation describes the ratio for reflected light as:

$$F = \frac{1}{2} * \left( \frac{\sin^2(\phi - \theta)}{\sin^2(\phi + \theta)} + \frac{\tan^2(\phi - \theta)}{\tan^2(\phi + \theta)} \right) \quad (3.18)$$

Usually an approximation of Fresnel is used as the exact Fresnel equation is quite complex. An approximation of Fresnel equation was given by Schlick [66] which has proven to be accurate for most materials.

$$F(\theta_i) = F_o + (1 - F_o)(1 - \cos(\theta_i))^5$$

$F_o$  is the measured Fresnel reflectance at normal incidence angle and  $\theta_i$  is the angle of incidence. Another frequently used approximation to the Fresnel term used is:

$$F = \frac{1}{2} \frac{(g-c)^2}{(g+c)^2} \left( 1 + \frac{[c(g+c)-1]^2}{[c(g-c)-1]^2} \right) \quad (3.19)$$

where  $c = \cos(\phi) = \vec{L} \cdot \vec{H}$ ,  $\eta$  is the index of refraction and  $g^2 = \eta^2 + c^2 - 1$ .

Since it is a microfacet based model, it uses the Beckman distribution [60] to define the microfacet orientation distribution by applying the Halfway vector to determine the overall roughness of the surface.

$$D = \frac{1}{\pi \cdot m^2 \cdot \cos^4 \cdot \alpha} \cdot e^{-(\tan \alpha / m)^2} \quad (3.20)$$

$\alpha$  is the angle between  $\vec{N}$  and  $\vec{H}$  and  $m$  is the root mean square slope of the microfacets. For small values of  $m$  the reflection becomes highly directional while for higher values of  $m$  the reflection is more spread out.

The geometric attenuation factor is given by:

$$G = \min \left\{ 1, \frac{2(\vec{N} \cdot \vec{H})(\vec{N} \cdot \vec{V})}{(\vec{V} \cdot \vec{H})}, \frac{2(\vec{N} \cdot \vec{H})(\vec{N} \cdot \vec{L})}{(\vec{V} \cdot \vec{H})} \right\} \quad (3.21)$$

$$G = \frac{2(\vec{N} \cdot \vec{H})(\vec{N} \cdot \vec{V})}{(\vec{V} \cdot \vec{H})} \quad (3.22)$$

$$G = \frac{2(\vec{N} \cdot \vec{H})(\vec{N} \cdot \vec{L})}{(\vec{V} \cdot \vec{H})} \quad (3.23)$$

Where 3.22 is the light blocked from the viewer and 3.23 is for the light considered to be in shadow. The geometric attenuation factor handles the shadowing and masking of the microfacets and calculates the resulting amount of light remaining after these effects. Its value ranges between 0 to 1 for completely shadowed(0) to no shadowing(1).

### Ward Model

The Ward reflectance model [79] is an empirical model that has been used for modelling of both isotropic and anisotropic reflection. Due to anisotropic reflection, the surface exhibits varying reflectance when it is rotated about the surface normal. This phenomenon is common in materials like: clothing (e.g. velvet), brushed steel, hairs etc. The BRDF is:

$$L(\omega_o, \omega_i) = \frac{\rho_d}{\pi} + \rho_s \frac{1}{\sqrt{\cos \theta_i \cos \theta_o}} \frac{\exp\left(-\tan^2 \theta_h \cdot \left(\frac{\cos^2 \phi_h}{\sigma_x^2} + \frac{\sin^2 \phi_h}{\sigma_y^2}\right)\right)}{4\pi \sigma_T \sigma_B}. \quad (3.24)$$

$\sigma_x$  and  $\sigma_y$  control the width of two lobes in two directions of anisotropy, while the lobe becomes isotropic when  $\sigma_x = \sigma_y$ .

For isotropic reflection the Ward BRDF is written as:

$$f_r(x, \omega_o, \omega_i) = \frac{\rho_d}{\pi} + \rho_s \frac{1}{\sqrt{\cos \theta_i \cos \theta_o}} \frac{\exp\left(-\frac{\tan^2 \theta_h}{\sigma^2}\right)}{4\pi\sigma^2}. \quad (3.25)$$

Several isotropic and anisotropic models also exist that try to model the complex interaction of light with materials. The choice of a reflectance function for a particular material however depends on the ability of a model to fit the actual reflectance of that material. Some of these models are good for real time shading due to their simplicity and computational cost, others are however intended for more realistic modelling for light interaction with different surfaces.

#### 3.1.1.4 Object Motion

Photometric stereo generally assumes that the object is static. Generally fast frame rate of camera or multi-spectral techniques are used to handle the artifacts of the motion but a handful of researchers have tried to improve motion artifacts by using other methods.

Decker *et al.* [24] presented a method for better optical flow registration for dynamic scenes by using the colour information. Their method allowed a fewer

number of frames over which optical flow must be computed in-order to handle dynamic scenes.

### **3.1.1.5 Light Source Direction**

Light sources in Photometric Stereo are normally assumed to be at infinite distance from the scene so that a homogeneous and parallel incident light condition can be formed and then the problem becomes solvable through a group of linear equations. In reality it is not always possible to produce parallel incident light, especially when the object size is big or the distance of the object from the light source is relatively small. Any underestimation or misalignment of the illumination may produce some error during recovery of the surface orientation. For example, a 1% uncertainty in the intensity estimation will cause a 0.5-3.5 degree deviation in the calculated surface normal for a typical three-light source photometric stereo setup [70]. Uncertainty in the calibration process can also lead to systemic errors when recovering surface normals and in the 3D recovered surface [49], [43]. It is also essential to have the best knowledge of the radiance distribution of the light sources when they are used to build the PS imaging setups. In the next chapter we have proposed a method to relax this restriction and improve the calculation of the light vector direction.

## 3.2 Photometric Stereo Setup and Data Acquisition

In order to capture high speed images and corresponding data from Spirometer, custom electronics and a rig was designed and built. The experimental setup is composed of two monochrome digital cameras 1.4 Mega pixel each and eight light sources. The rig is composed of two identical sub-rigs placed opposite to each other. Each sub-rig has one camera and four light sources as shown in the Figure 3.2. The subject stands in middle of the rig wearing a white tight t-shirt and is asked to do diaphragmatic breathing. Current light sources used are single wavelength blue light. Corresponding band pass filters are used to suppress the background light in the room.

The system is designed so that it can run using an ordinary office desktop computer. Timing of the lighting and the camera trigger are controlled using an FPGA board [54]. Custom embedded software for FPGA was designed using VHDL. The cameras are directly connected to the computer using Gigabit Ethernet cards. To get ground-truth data, analog pneumotachometers and transducers are used. The signal from the transducer is digitized using a 12-bit analog to digital converter on a custom designed board and stored on a FPGA board. The overall block diagram of the hardware setup is shown in Figure 3.3.

Images are captured in raw binary format and stored on a high speed solid

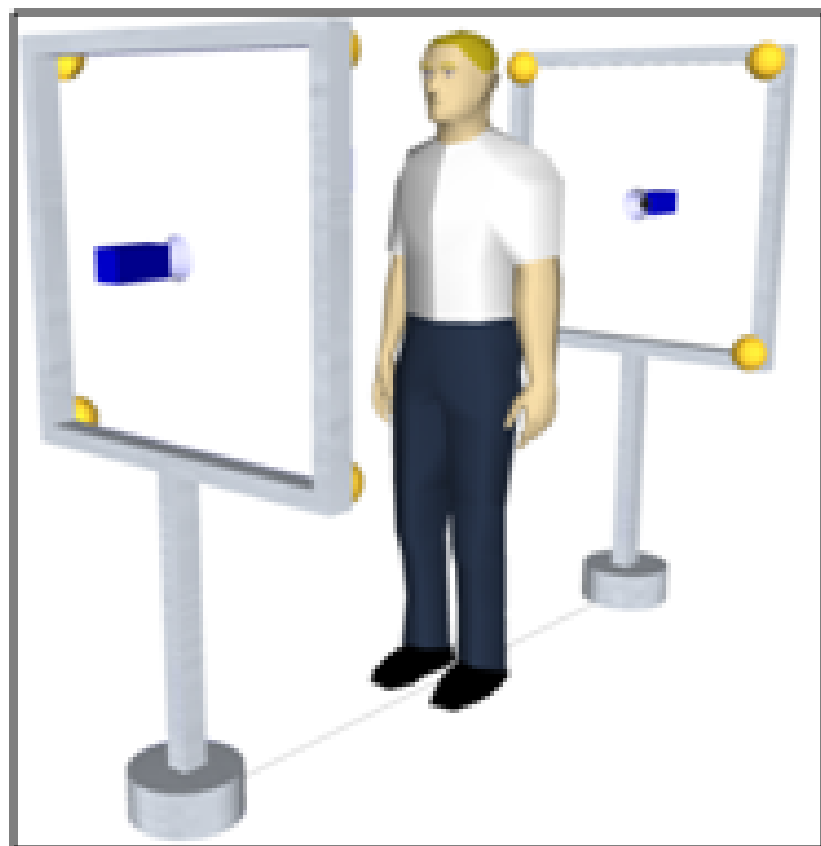
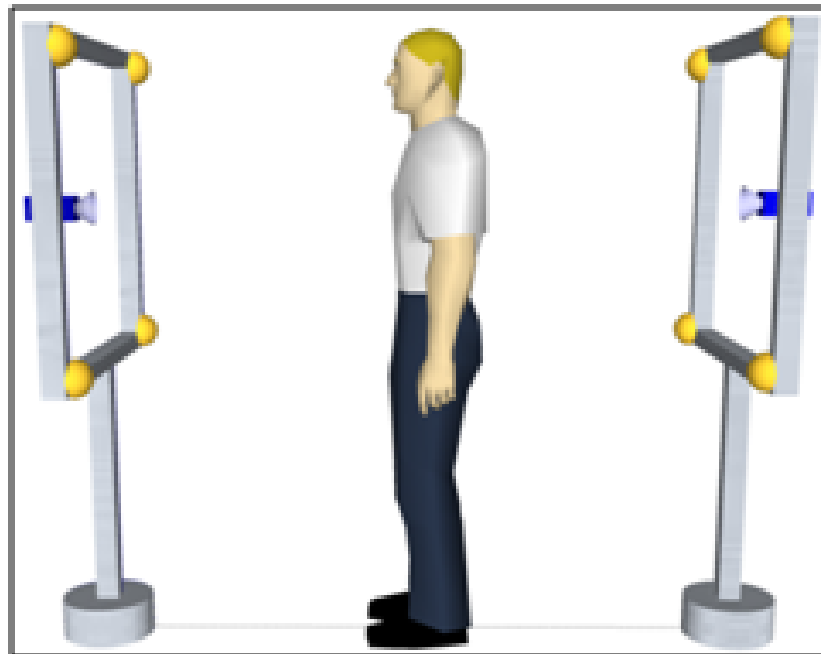


Figure 3.2: Photometric stereo rig with subject standing in middle of rig

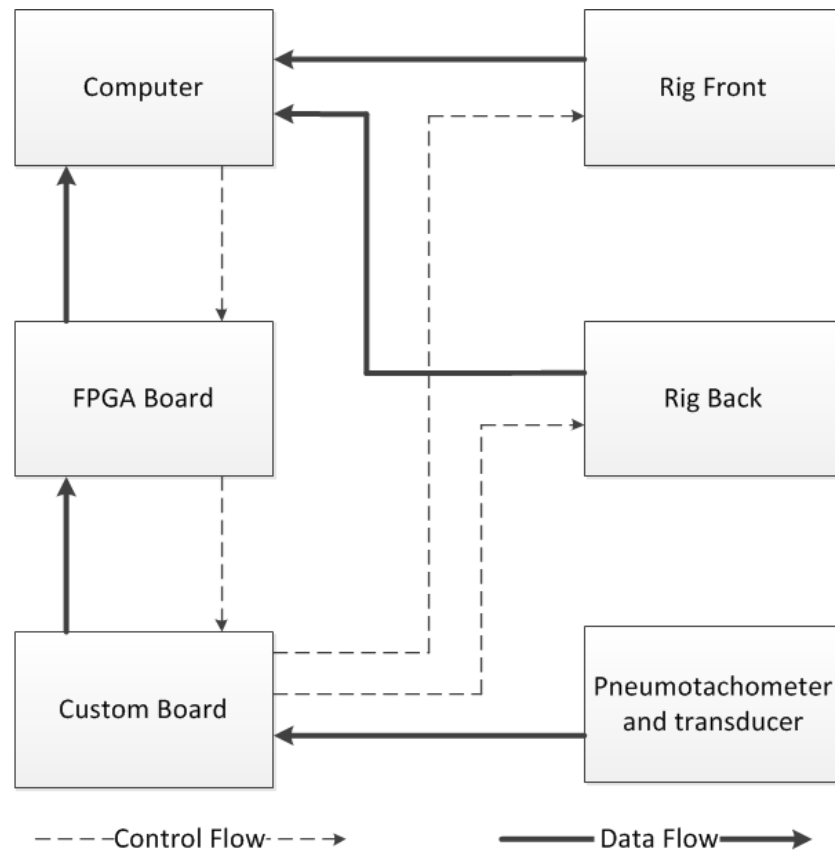


Figure 3.3: Block diagram of Hardware. Dotted arrows represent flow of camera trigger and light source power flow. Solid arrows represent flow of raw images and signal obtained from Pneumotachometer.

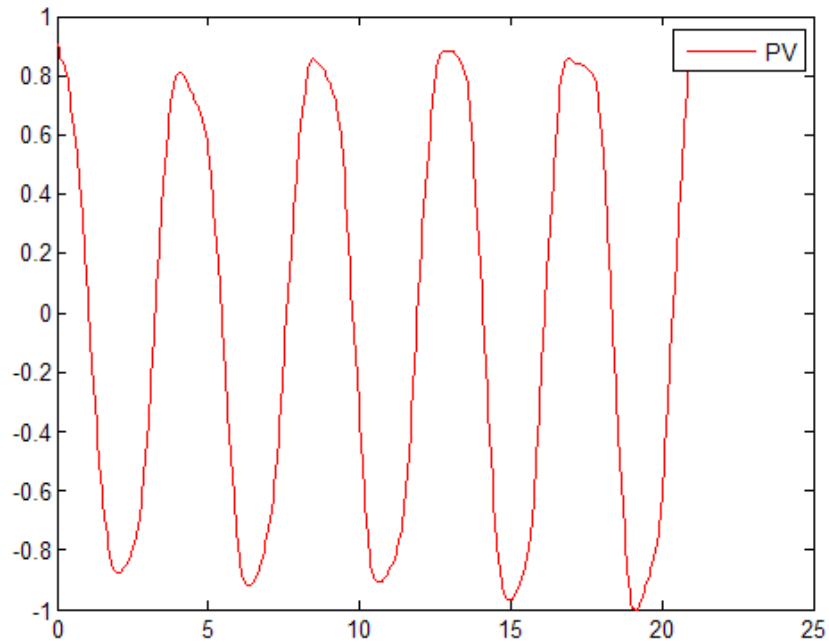


Figure 3.4: Pneumotachometer volume (PV) signal obtained after digitization. Horizontal axis is time in seconds. Vertical scale is a normalized unit less representation of volume, to compare volume obtained from Pneumotachometer and Gradient.

state drive. Once the data acquisition is done the captured images are transferred onto an ordinary hard disk for processing. A high speed FPGA based embedded system is designed to precisely control the timing for camera triggering and lighting. Currently the system is capable of capturing at 110 FPS without any image losses, for around 10 minutes. This restriction of 10 minutes can be reduced by using a bigger solid state drive. The custom board samples the pneumotachometer data at the rate of 1000 samples per second. A typical Pneumotachometer volume (PV) signal is shown in Figure 3.4.

To estimate surface gradient, Photometric Stereo requires at least three images taken from the same view point but with different light directions. In our

setup we use five images to estimate surface gradient. Four images are taken by turning on one light source at a time as shown in Figure 3.5(a) to Figure 3.5(d). Light sources are placed at equal distance from each other to get homogeneous light distribution among all four images as shown in Figure 3.2. The fifth image is taken when no light source is turned on to get the background light intensity (noise) as shown in Figure 3.5(e). All images are taken in unconstrained room environment a light on ceiling is visible in Figure 3.5(e). This room noise is removed using background subtraction. By using a circular shift method we are able to generate 3D data (surface gradient) at 44 fps for the whole torso.



(a) (b) (c) (d) (e)

Figure 3.5: Raw Images obtained from Front Rig. Image(a) when top-right light is turned on, image(b) when bottom-right light is turned on, image(c) when bottom-left light is turned on, image(d) when top-left light is turned on and image(e) is when no light is turned on.

### 3.3 Volume calculation from photometric stereo

The volume of the torso is represented as the total average gradient; we call it the gradient volume ( $GV$ ).  $GV$  is calculated by adding the absolute average of  $p$  and  $q$  and then normalizing it as shown in equation 3.26 and equation 3.27 for both front and back.

$$V = \frac{1}{k} \sum (|p_f| + |q_f|) + \frac{1}{l} \sum (|p_b| + |q_b|) \quad (3.26)$$

Where  $k$  and  $l$  are the total number of valid pixels in the front and back images respectively,  $p_f$ ,  $q_f$  are the local surface gradients of front image and  $p_b$ ,  $q_b$  are the local surface gradients of the back image. To compare the  $GV$  with the volume obtained from Pneumotachometer normalization is applied on both signals using equation 3.27.

$$GV = \frac{V - [\frac{1}{t} \sum V]}{\max(|V - [\frac{1}{t} \sum V]|)} \quad (3.27)$$

Here  $t$  represents total values in the temporal domain. A typical  $GV$  signal obtained from the method explained above and normalized by equation 3.27 is shown in Figure 3.6.

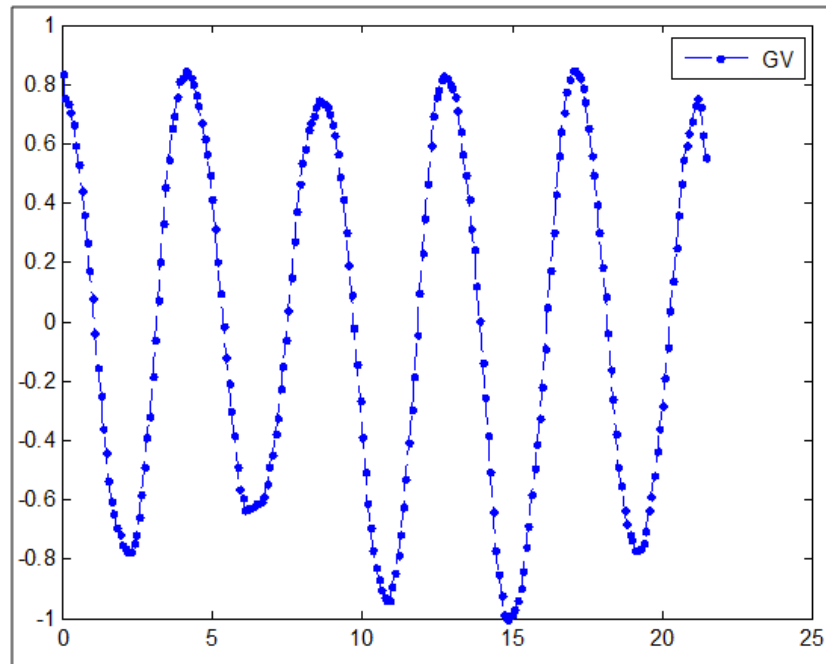


Figure 3.6: Volume obtained from surface gradient (GV). Horizontal axis is time in seconds. Vertical scale is a normalized representation of volume, to compare volume obtained from Pneumotachometer and Gradient.

High correlation (0.98) between gradient volume and Pneumotachometer volume (Ground Truth) was found as shown in Figure 3.7. It also reflects that the effect of the error in surface gradient is very minimal on volume calculation because of the normalization and calibration processes used to calculate the relative and absolute amount of air.

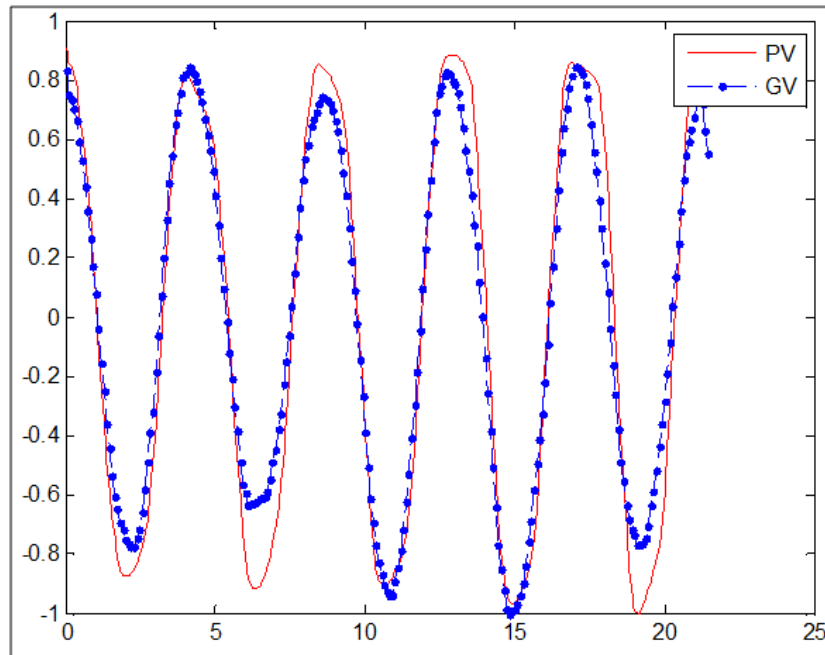


Figure 3.7: Comparison of Pneumotachometer Volume (PV) and Gradient Volume (GV) (combined front and back). Horizontal axis is time in seconds. Vertical scale is a normalized representation of volume.

### 3.4 Conclusion

Photometric Stereo based pulmonary functional testing system is developed and initial experiments showed that the volume signal is highly correlated to the traditional spirometer. The volume signal can be obtained using the gradient calculated from photometric stereo images. However there are a few assumptions and limitations regarding photometric stereo. Some of the assumptions can be handled by using proper calibration and by wearing a white t-shirt. However pho-

tomeric stereo does not provide any information about the absolute distance of the object from camera or the absolute dimensions of the object. To obtain the absolute amount of air, a new distance calculation method is proposed in next chapter. A light vector direction improvement method is also proposed in the next chapter.

## **Chapter 4**

# **An Improved Photometric Stereo Through Distance Estimation And Light Vector Optimization From Diffused Maxima Region**

In this chapter photometric stereo is discussed in detail. Light vector direction for Photometric Stereo is improved by employing Diffused Maxima Region. Distance of object from camera is first calculated and then used to improve the direction of light vectors. In later chapter we use this distance information to obtain the absolute amount of air from the initial experimental results.

## 4.1 Introduction

Traditional Photometric Stereo (PS) recovers the surface shape of an object or scene by using several images taken from the same view point but under different controlled lighting conditions [14, 71, 82]. It has been extensively used in many applications [2, 3, 37, 38, 42, 46, 56], especially for estimating high density local surface orientation in the fields of computer vision and computer graphics. However the 3D reconstructions from the recovered surface orientation are prone to low frequency geometric distortion because the real illumination is unable to satisfy the assumed, ideal conditions under which PS works [43].

Light sources in PS are normally assumed to be at infinite distance from the scene so that a homogeneous and parallel incident light condition can be formed and then the problem becomes solvable through a group of linear equations. In reality it is not always possible to produce parallel incident light, especially when

the object size is big or the distance of object from light source is relatively small. Any underestimation or misalignment of the illumination may produce some error during recovery of the surface orientation. For example, a 1% uncertainty in the intensity estimation will cause a 0.5-3.5 degree deviation in the calculated surface normal for a typical three-light source photometric stereo setup [70]. Uncertainty in the calibration process can also lead to systemic errors when recovering surface normals and in the 3D recovered surface [49], [43]. It is also essential to have the best knowledge of the radiance distribution of the light sources when they are used to build the PS imaging setups.

Furthermore PS gives no information concerning the absolute distance of the object from the camera. Another additional imaging modality is normally required for obtaining the range data, for example laser triangulation or stereo vision techniques have been combined with the PS approach [23, 26, 39, 47, 83].

In this chapter we present a novel method for calculating the distance of an object using the photometric stereo imaging setup and then use this additional information to improve accuracy of surface normal estimation by calculating per-pixel light direction rather than assuming same light direction for every pixel. Using only one camera and four lights without a requirement for any additional hardware, and with only little extra processing cost, the object's distance from the camera is esti-

mated by finding the diffused maxima region (DMR). DMR is a small patch on the object surface whose normal is pointing towards the light source [16, 29]. From this the estimated distance is used to calculate the light vectors at every image pixel thereby minimizing the error associated with the assumption of collimated light source. This allows the photometric stereo method to work with real light sources, on Lambertian surfaces that have at least one small patch with normal vectors pointing directly towards the light.

## **4.2 Background and related work**

The common low cost approach to produce collimated light is to use convex lenses or concave mirrors; but even in these cases, only a narrow parallel light beam with a similar physical size to that of the lens or mirror can be obtained. To produce a collimated light source for a larger scene area, a possible solution is to develop a custom optical system with an array of specially aligned individual light units. Unfortunately this results in a high hardware and setup cost [68]. Another practical solution is to set the light sources far away from the object [11], so that the light can be approximated as a distant radiation point source. This strategy may help to provide evenly distributed radiance across the object surface, but it sacrifices the majority of the illumination intensity, and correspondingly de-

creases the signal/noise ratio of the whole system. In addition, such a distant lighting setup usually means a large impractical working space is required. So this approach is only suitable for those light sources able to produce high levels of energy and those applications where a large redundant space is available. In terms of the availability and flexibility of current commercial illumination, the distant illumination solution is often not an optimal choice.

A nearby light source model has been considered as an alternative by Kim [48] and Iwahori [44] to reduce the photometric stereo problem to find a local depth solution using a single non-linear equation. By distributing the light sources symmetrically in a plane perpendicular to camera optical axis, they were able to get a unique solution of non-linear equations. However, selection of initial values for the optimisation process and limitations in the speed for solving non-linear equation are the main problems with this method.

A moving point light source based solution has been proposed by Clark [21] termed "Active Photometric Stereo". By moving a point light along a known path close to the object surface a linear solution can be formulated to solve the photometric stereo problem. However, the range of motion of light must be closely controlled in order to guarantee the efficiency of the solution.

Kozera and Noakes introduced an iterative 2D Leap-Frog algorithm able to

solve the noisy and non-distant illumination issue for three light-source photometric stereo [51]. Because distributed illuminators are commercially available, Smith *et al.* approximated two symmetrically distributed nearby point sources as one virtual distant point light source for their dynamic photometric stereo method [69]. Unfortunately, none of these methods lend themselves to a generalized approach.

Varnavas *et al.* [74] implemented parallel CUDA based architecture and computed light vectors at each pixel, so that a changing light direction was taken into account. However in practice the whole surface is not necessarily at the same distance from the light source, especially when the size of the object is comparable to the distance of the light source.

### **4.3 Proposed Method**

By estimating the distance of the object from the camera we can improve the accuracy of the surface normals by calculating the light vector of every pixel based on its distance from the camera and light source. The proposed method is summarised in Pseudo code in Table 4.1. It is divided into three parts: “Light source position estimation”, “Object distance estimation” and “Per pixel light direction calculation”. Light source position estimation is required only once during the rig

calibration process.

### 4.3.1 Light source position estimation

The general assumption that the light vector is the same at every point (pixel) is mostly not true in practice, so subsequently we use triangulation and the intersection of at least two light vectors (calculated at different positions) to determine the true position of a light in a world coordinate system at the optical centre as shown in Figure 4.1. A specular sphere is used to calculate the light vectors at several (we take two as example) different locations in the imaging area. The intersection of these light vectors is taken as the position of the light in the real world coordinate system. The position of light 1 is calculated by finding the intersection point of light vectors  $\vec{L}_1$  and  $\vec{L}_2$  as shown in Figure 4.1.  $\vec{L}_1$  is the light vector calculated at a sphere surface position  $p_1^1$  by placing the sphere at one random location and  $\vec{L}_2$  is the light vector calculated at a sphere surface position  $p_2^1$  by placing the sphere at another random location in the imaging area. To calculate  $\vec{L}_1$  and  $\vec{L}_2$  Equation 4.1 is used.

$$\vec{L} = 2(\vec{n} \cdot \vec{d})\vec{n} - \vec{d} \quad (4.1)$$

Where  $\vec{d}$  is reflection direction taken as (0,0,1),  $\vec{n}$  is unit surface normal at

Table 4.1: Pseudo code of proposed method.

<p><b>1. Light Source Position Estimation.</b></p> <p>1.1. Place a specular sphere in Field of view.</p> <p>1.2. Calculate Light vector using equation 4.1.</p> <p>1.3. Calculate position of the highlight point in world coordinates using equation 4.12.</p> <p>1.4. Repeat steps 1.1 to 1.3 by placing the sphere in another location.</p> <p>1.5. Once two light vectors and two highlight positions for the same light has been calculated using the above steps, the position of light can be calculated using equation 4.4.</p> <p>1.6. Repeat steps 1.1 to 1.5 for all light sources to calculate light positions.</p> <p>1.7. Calculate light vectors of all lights by placing the sphere in the centre of field of view by using equation 4.1. These light vectors will be called pseudo light vectors.</p>
<p><b>2. Object distance estimation.</b></p> <p>2.1. Capture a sequence of images of the object.</p> <p>2.2. Calculate surface normals by using pseudo light vectors and equation 3.6. Resultant normals are called pseudo normals.</p> <p>2.3. Calculate diffused maximum region by using equation 4.13.</p> <p>2.4. Create a vector from centre of diffused maximum region to centre of lens as shown in Figure 4.3(a).</p> <p>2.5. Now using origin of lens, pseudo light vector, position of light and vector created in step 2.4 we can calculate distance of object by using the same intersection equations as used in step 1.5.</p> <p>2.6. Repeat steps 2.2 to 2.4 for every light source and take average of all estimated distance values for final estimated value.</p>
<p><b>3. Per pixel light direction calculation.</b></p> <p>3.1. Draw an imaginary plane at the estimated distance.</p> <p>3.2. Calculate vectors from light position to every pixel on the plane to obtain per-pixel light vectors.</p>

point  $p_1^1$  or  $p_2^1$ ,  $\vec{n} = (nx, ny, nz)$ ,  $nx = px - cx$ ,  $ny = py - cy$  and  $n_z = \sqrt{(r^2 - n_x^2 - n_y^2)}$ ,

$(cx, cy)$  and  $(px, py)$  are the pixel coordinates of the sphere centre and the highlight

on the sphere respectively, and  $r$  is the radius of sphere in the image plane.

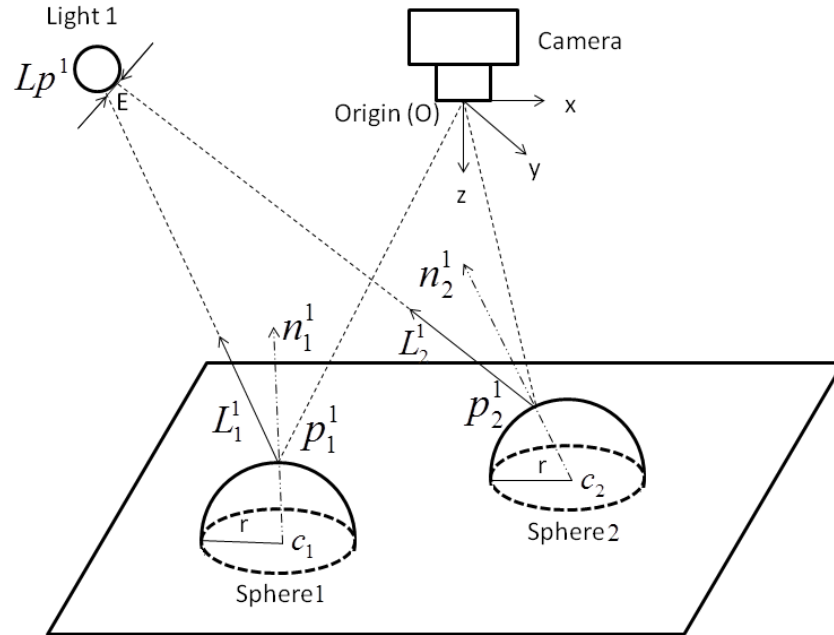


Figure 4.1: Calibration setup for light position calculation and initial (Pseudo) light vector calculation.

The intersection of  $\vec{L}_1^1$  and  $\vec{L}_2^1$  can be calculated using equations 4.2, 4.3 and

4.4 [27]

$$Lp_1^1 = p_1^1 + \left( \frac{(\vec{L}_2^1 \times (p_1^1 - p_2^1)) \cdot (\vec{L}_1^1 \times \vec{L}_2^1)}{(\vec{L}_1^1 \times \vec{L}_2^1) \cdot (\vec{L}_1^1 \times \vec{L}_2^1)} \right) * \vec{L}_1^1 \quad (4.2)$$

$$Lp_2^1 = p_2^1 + \left( \frac{(\vec{L}_1^1 \times (p_1^1 - p_2^1)) \cdot (\vec{L}_1^1 \times \vec{L}_2^1)}{(\vec{L}_1^1 \times \vec{L}_2^1) \cdot (\vec{L}_1^1 \times \vec{L}_2^1)} \right) * \vec{L}_2^1 \quad (4.3)$$

$$Lp^1 = \frac{Lp_1^1 + Lp_2^1}{2} \quad (4.4)$$

$$E = |Lp_1^1 - Lp_2^1| \quad (4.5)$$

$Lp^1$  is the 3D position of light 1 in the world coordinate system.  $Lp_1^1$  is the point on vector  $\vec{L}_1^1$  closest to  $\vec{L}_2^1$ ,  $Lp_2^1$  is the point on vector  $\vec{L}_2^1$  closest to  $\vec{L}_1^1$ ,  $E$  is the distance between these two points - which can be used to measure the accuracy of the calculation. If  $E$  is zero then both light vectors intersect. However, due to error in estimating the light vector, the position of the highlight or sphere centre  $E$  is not always zero or close to zero. So we use a threshold to establish when the estimated light position is not accurate. In this case the sphere can be positioned in additional places to improve the accuracy.

To calculate the position of light using the above method we need the position of at least two highlights on the sphere surface. These highlights can be calculated by first calculating the centre of the sphere. As the actual size of the sphere, focal length of the camera and physical pixel size of camera sensor are known, we can find the position of the centre of the sphere in the world coordinate system.

$$C(X, Y, Z) = \left[ \frac{-x}{f_x} Z, \frac{-y}{f_y} Z, Z \right] \quad (4.6)$$

$$Z = \frac{\text{focal length} * \text{sphere actual radius}}{\text{pixel length} * \text{sphere pixel radius}} \quad (4.7)$$

Where  $Z$  is the distance of sphere centre from camera in the z-direction,  $f_x$  and  $f_y$  are the focal length in pixels in  $x$  and  $y$  direction. Once the centre of sphere  $C$  is known, the surface normal  $\vec{n}$  at point  $P$  (highlight pixel position) can be used to calculate  $P$  from equation 4.8.

$$P(X, Y, Z) = C(X, Y, Z) + k * n(X, Y, Z) \quad (4.8)$$

$k$  is a constant required to calculate  $P$ . As  $P$  lies on the surface of the sphere  $|P - C|$  should be equal to the sphere radius and by using value of  $P$  from equation 4.8 we can solve the value of  $k$  from the following equations.

$$|c + k\vec{n} - c| = \text{sphere actual radius} \quad (4.9)$$

$$|\vec{n}| = 1 \quad (4.10)$$

$$k = \text{sphere actual radius} \quad (4.11)$$

Once the value of  $k$  is calculated, it can be used in equation 4.8 to calculate the position of the highlight on the sphere surface in real world coordinates; as shown in equation 4.12.

$$P(X,Y,Z) = C(X,Y,Z) + (\text{sphere actual radius}) * \vec{n} \quad (4.12)$$

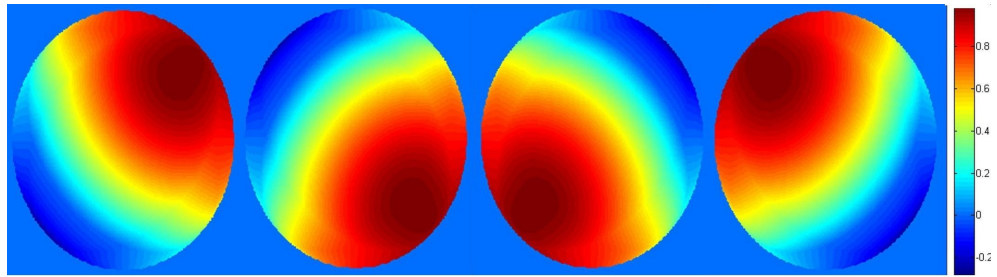
### 4.3.2 Object Distance Estimation

The object distance from the camera is calculated by using the Diffused Maxima Region (DMR), which is calculated by taking the absolute value of the dot product between the pseudo light vector and pseudo surface normal, and then applying a threshold; as shown in equation 4.13. During experimentation we have found that for most cases the threshold is greater than or equal to 0.9.

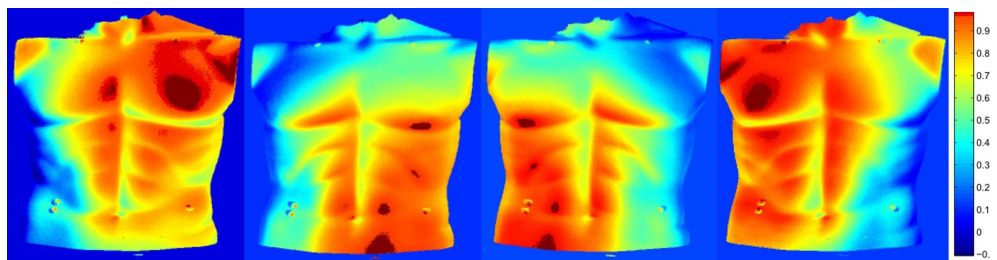
$$DMR_i = |\vec{N} \cdot \vec{L}^i| \geq 0.9 \quad (4.13)$$

$\vec{L}^i$  is a pseudo light vector for light  $i$  and  $\vec{N}$  is the pseudo surface normal at each pixel. The pseudo light vector  $\vec{L}^i$  is calculated during the calibration process

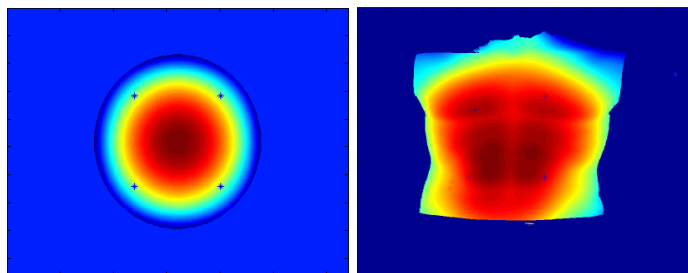
by placing the sphere at the centre of the field of view, it is assumed to be the same for every pixel. The centre of the *DMR* gives us the point where the surface normal and the light vector are approximately aligned. Many  $DMR(s)$  can exist on the surface of an object but the region with maximum pixel area is considered to be the best choice. Lights are arranged in a square arrangement as shown in Figure 4.4(a) and the dot product of the light vectors with surface normals are shown in Figure 4.2. Higher value of dot product means it is closer to the diffused maxima. Figure 4.2 shows the four selected *DMR* centres plotted on a height map of a synthetic sphere and a real human dummy torso.



(a)



(b)



(c)

(d)

Figure 4.2: (a) and (b) dot product of image with its light vectors. Diffused maxima regions are highlighted in dark red colour. (c) and (d) Diffused Maxima Regions centres are plotted on Height Map

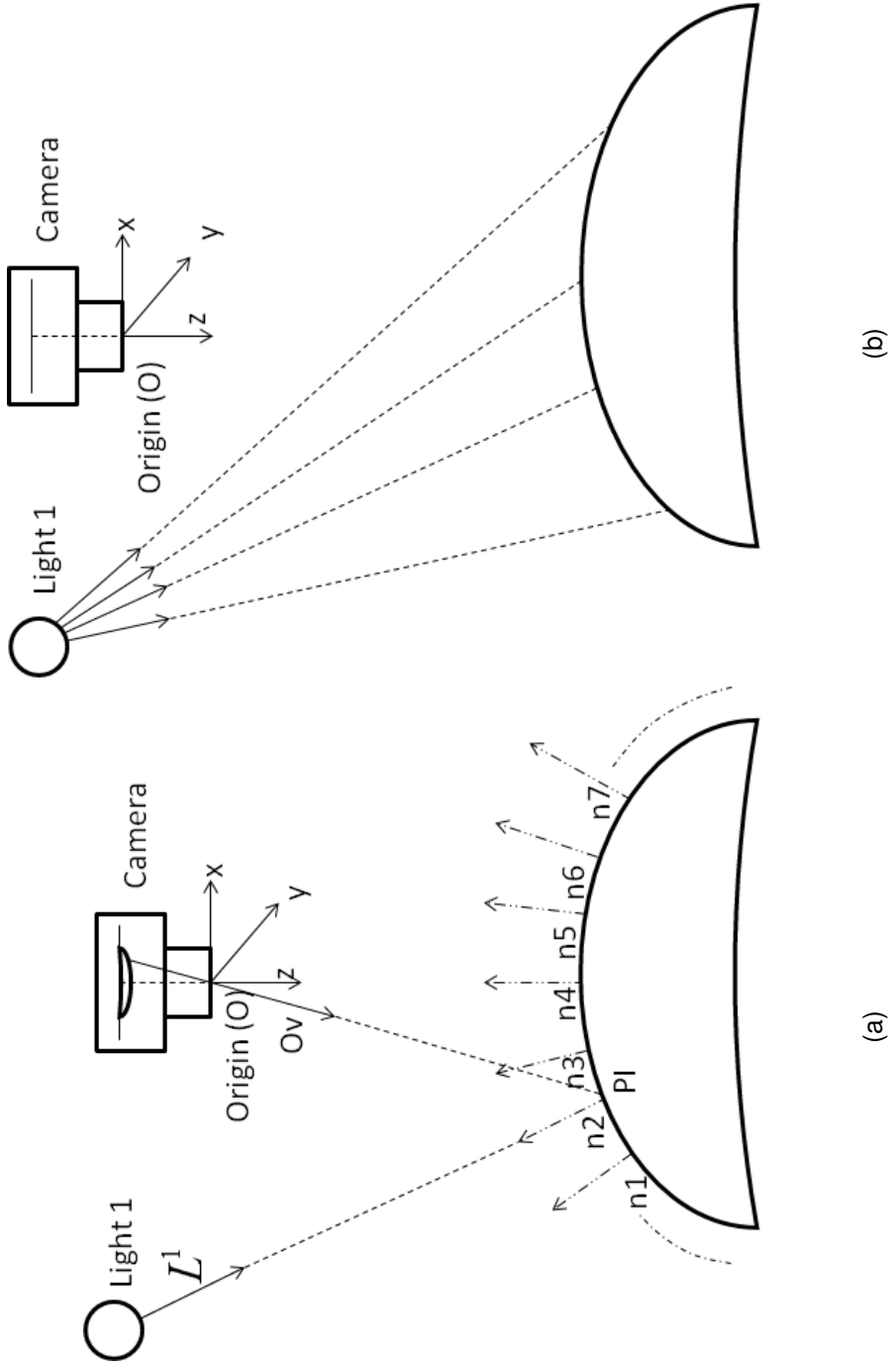


Figure 4.3: (a) Depth calculation using DMR and intersection of vector  $O_v$  and  $L^1$ . (b) Light vector calculation on each point of object surface.

Once the *DMR* centre is identified in the image plane, a vector  $\vec{Ov}$  can be created from the *DMR* centre to the centre of the lens  $O$ , as shown in Figure 4.3(a).  $O$  is also the origin of the world coordinate system. Now by using origin  $O$ , position of light  $LP$ , light vector  $\vec{L}^1$  and vector  $\vec{Ov}$ , we can determine the intersection point of these two vectors in world coordinates by using equations 4.2, 4.3 and 4.4. The average of the  $Z$  coordinate of these points of intersection is the estimated distance of the object from the camera.

### 4.3.3 Per pixel light direction calculation

Once the distance of the object is known from the camera, an imaginary plane parallel to the image plane is created. The pseudo height of the object is then defined relative to this plane by adding the reconstructed surface from pseudo normals; so that new light vectors for each pixel point for each light are created as shown in Figure 4.3(b). The pseudo height of the object is calculated by integrating [67] the pseudo surface normal  $N$  and then scaling the height to compensate for the camera distance.

Traditional photometric stereo assumes that the light direction is the same across the whole scene but in reality, particularly where the object has a comparable size to the illumination working distance, it is clear that this varies; as

shown in Figure 4.3(b). This variation needs to be considered for accurate surface normal calculation because any variations in the illumination position are finally interpreted as uncertainty in recovered surface normals. For our synthetic imaging setup Table 4.2 shows the range of light vectors in terms of tilt and slant of a plane at a known distance from the camera, compared to traditional photometric stereo where the tilt and slant angle of illumination are normally assumed fixed.

Table 4.2: Tilt and Slant Light angle range for traditional PS and proposed method

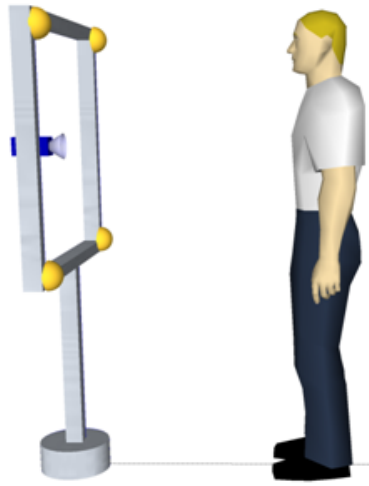
	Our Method		Traditional PS	
	Max/Min Tilt(degree)	Max/Min Slant(degree)	Tilt (degree)	Slant (degree)
Light 1	-8.8/-76.2	83.3/57	-45	70.5
Light 2	171.2/103.8	83.4/57.2	135	70.5
Light 3	-103/-171	83/57	-135	70.5
Light 4	70.5/8.8	83/57	45	70.5

## 4.4 Experiments

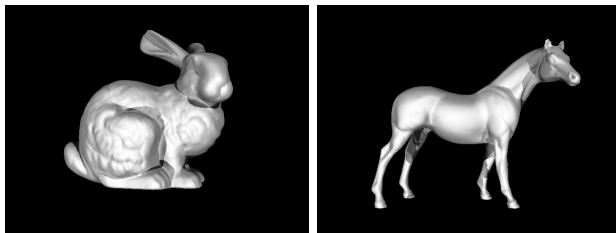
Experiments were performed on a range of synthetic images as well as with real images. For real images a setup based on a Teledyne DALSA Genie HM1400 1.4 Mega pixel monochrome camera and High power LEDs was designed as shown in Figure 4.4(a). A commercial 3dMD [1] system is used to acquire ground truth data as this system has a reported 0.2 mm accuracy in depth measurement.

3dMD is a commercial system which uses stereo vision to calculate disparity between two images and construct the 3D shape of the object. In order to calculate disparity, pixels from one image are matched with second image this corresponding problem is very well known in machine vision literature. This is a resource intensive task. To simplify this, 3dMD projects a known pattern onto the objects during capture to allow easier point matching. The advantages of such technique are high accuracy and fast acquisition times. However, the processing time is approximately 90 sec to reconstruct a small object on a modern desktop computer. This type of system is also expensive, requires a time consuming calibration procedure, and omits fine details such as wrinkles and pores as well as struggling with hair.

Figure 4.5(a) shows the error (mm) in the calculation of object distance from camera when the initial calibration (pseudo light vectors) of the setup is performed

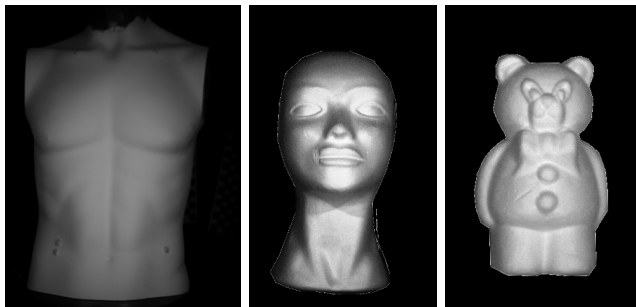


(a)



(b)

(c)



(d)

(e)

(f)

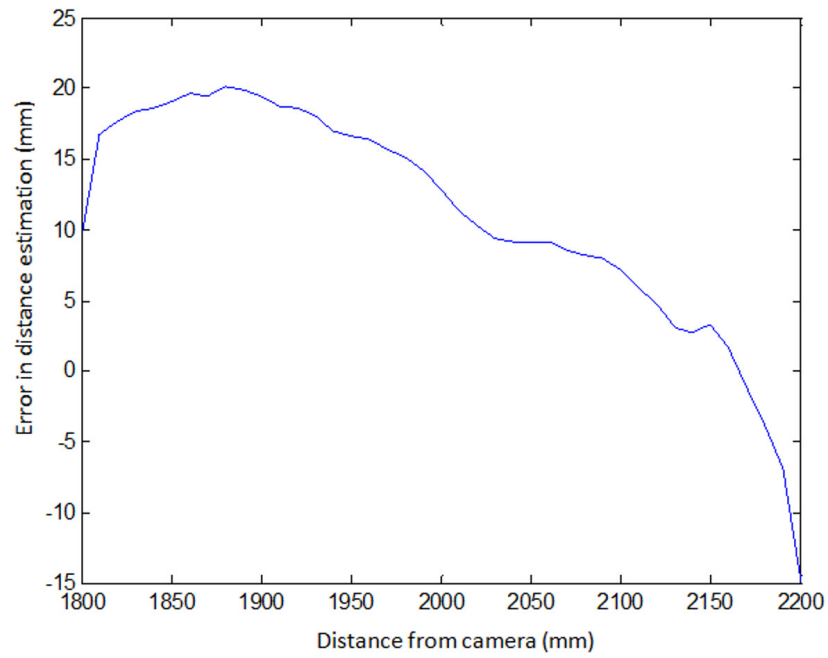
Figure 4.4: (a) Image acquisition Setup. (b-f) images of Objects used in Experiments

with the specular sphere located approximately at 2000 mm from the camera. The  $\sim \pm 20$  mm uncertainty is found when the object is moved from 1800 mm to 2200 mm from the camera. This is relatively high compared to other 3D range finding technologies, however the system can achieve a recovery in pixel level which is not provided by any other 3D imaging systems.

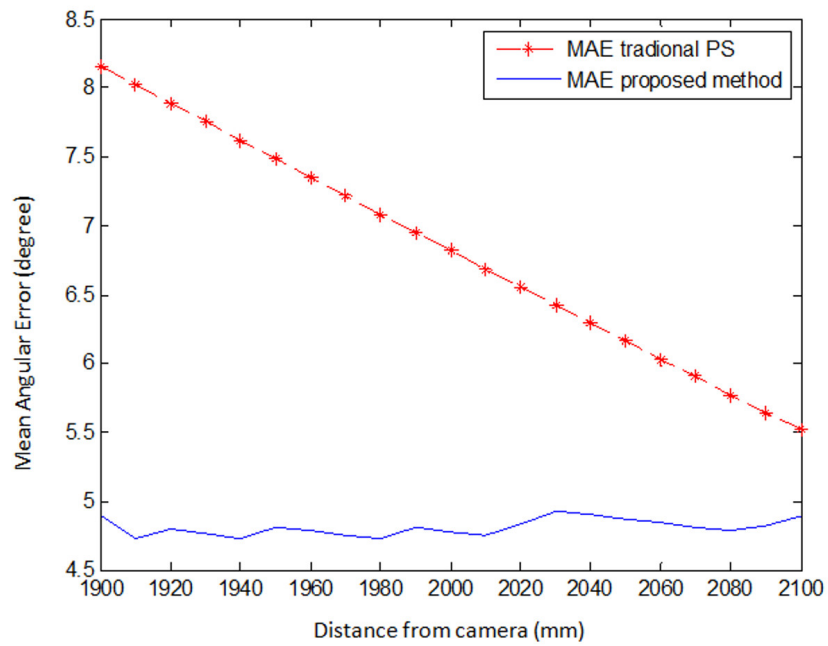
## 4.5 Results

This chapter has presented a method to enable light vectors to be calculated dynamically (as an object moves in field of view) for improving photometric stereo 3D surface reconstruction performance. Traditional Photometric Stereo assumes that light vectors at every pixel are the same, which is not usually the case in real applications, and especially where the object size is comparable to object range. The error in estimating the surface normals is highly dependent on the placement of the calibrated object relative to the camera. By using the proposed method this error is reduced and almost constant and independent from the working distance.

To test the accuracy of the surface normals acquired from the proposed method we have used Mean Angular Error (MAE) as the measure of accuracy. MAE is calculated by taking the cosine inverse of the dot product of a ground truth surface normal and a calculated surface normal. Table 4.3 summarises the Mean Angu-



(a)



(b)

Figure 4.5: (a) Absolute Error in distance estimation from camera to object. (b) Mean angular error in surface normals.

lar error calculated from synthetic as well as real images. Table 4.3 shows that the mean error in the height calculation of the reconstructed surface is improved around 2-6 mm in height and there is around 2-3 degree improvement in surface normal estimation.

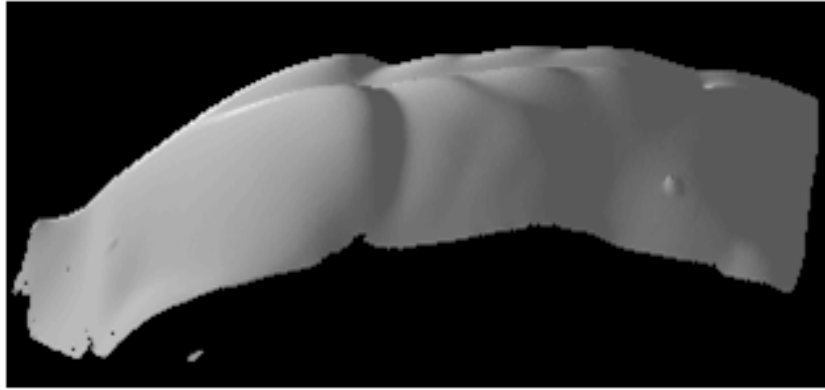
Figure 4.5(b) shows mean angular error (degrees) when the object is moved from 1900 mm to 2100 mm with the initial light vector for traditional photometric stereo and a pseudo light vector for our proposed method calculated at 2000 mm. It can be found that the MAE in traditional photometric stereo is highly dependent on the location of object with respect to the calibration position while the proposed method has a constant low MAE.

Table 4.3: Mean Error

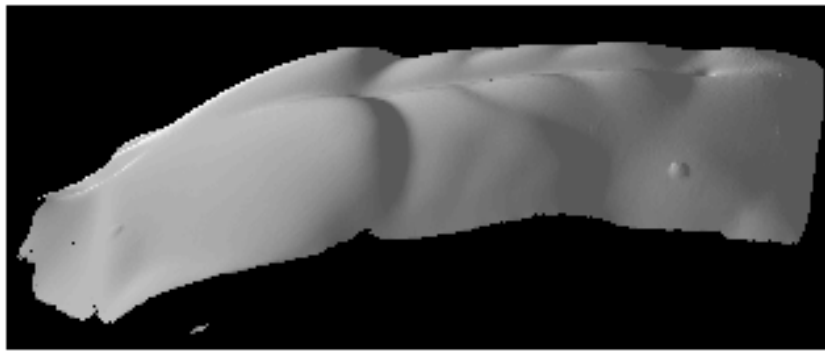
Object		Mean Angular Error in surface normal (degree)			Mean Height Error (mm)		
Name	Size (mm)	Traditional PS [82]	Our Method	Improvement	Traditional PS[82]	Our Method	Improvement
Synthetic Sphere	700x700	6.53	4.53	2.0	14.586	9.108	5.478
Synthetic Bunny	700x700	3.95	2.36	1.59	15.378	11.826	3.552
Synthetic Horse	700x700	3.90	2.33	1.57	9.174	6.608	2.566
Polystyrene Sphere	100x100	6.72	4.61	2.11	15.642	10.714	4.928
Human Dummy	650x450	6.88	4.86	2.02	17.006	11.066	5.94
Polystyrene Face	250x100	7.1	5.2	1.9	15.642	13.530	2.112
Polystyrene Owl	150x100	7.5	4.18	3.32	15.224	11.044	4.18

Figure 4.6(a) shows the surface reconstructed from surface normals obtained from traditional photometric stereo while Figure 4.6(b) is the surface reconstructed from surface normals obtained from the proposed method by using a Poisson based surface integrator [67]. If we visually compare Figure 4.6(a) with the ground truth in Figure 4.6(c) we can easily find low frequency geometric distortion in addition to high frequency noise. This geometric distortion is due to the fact that photometric stereo in its original form interprets a change in light intensity due to change in light direction as change in surface normal, which is very common in low cost and large field of view photometric stereo imaging setups. In comparison, Figure 4.6(b) is more flat and closer to the ground truth. This is because the geometric distortion is partially removed by considering the lighting distance from the object surface. The same phenomena can be observed clearly by plotting slices of the surfaces as shown in Figure 4.7.

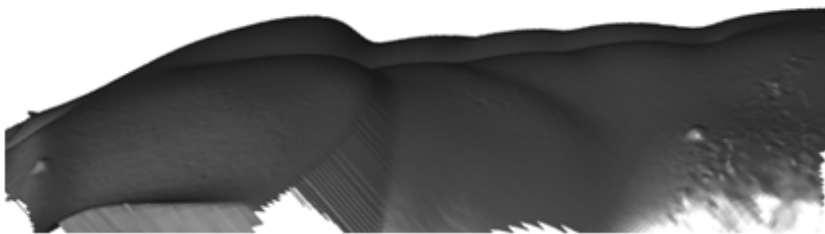
Figure 4.7 shows slices of reconstructed surfaces. When comparing the proposed method, with traditional photometric stereo, it is clear that the proposed method calculates more accurate surface normals and hence better surface reconstruction.



(a)

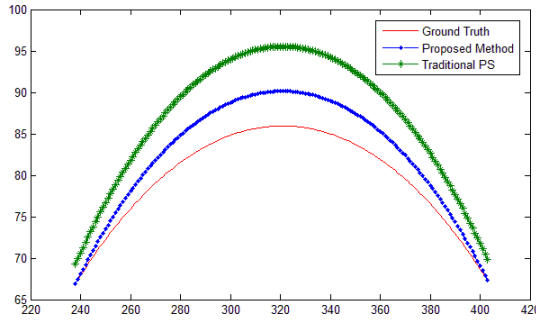


(b)

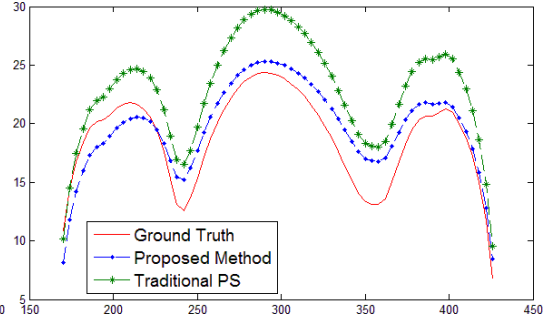


(c)

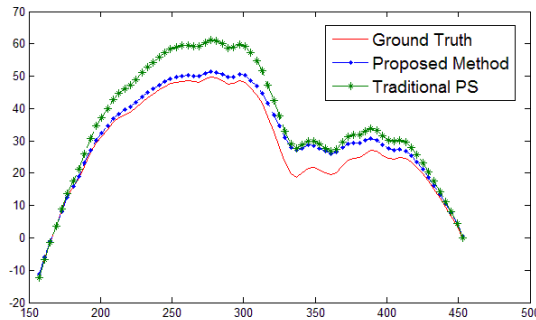
Figure 4.6: (a) Integrated surface using traditional PS. (b) Integrated surface using Proposed method. (c) Surface scanned from 3dMD as a ground truth.



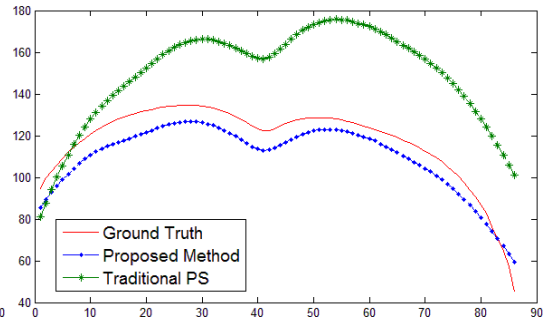
(a) Synthetic Sphere



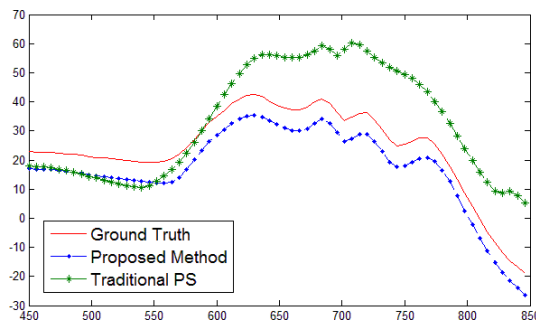
(b) Synthetic Horse



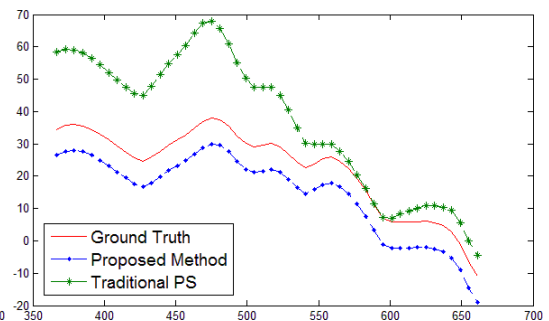
(c) Synthetic Bunny



(d) Human Torso Dummy



(e) Polystyrene Face



(f) Polystyrene Owl

Figure 4.7: Slices of integrated surface

## 4.6 Conclusion

In this chapter a novel method for distance calculation is presented. Proposed method uses fact that objects in nature are convex shaped and at-least on patch of surface exists on the whole surface who's normal is pointing towards the light direction. Several such points are detected on the surface and then distance of object from camera is estimated to help improve the surface normal's accuracy. In-addition of improved surface normal this method produces distance of object from camera as by-product which is used in later chapters for converting relative breathing signal to absolute breathing signal.

## **Chapter 5**

# **Non-Contact Pulmonary Functional Testing through an improved Photometric Stereo Approach**

The technique used for the preliminary results of photometric stereo based Pulmonary functional testing, presented in chapter 3, is further extended in this chapter to calculate the absolute amount of air. It utilizes the distance calculation method developed in previous chapter. Distance of object calculated using Diffused Maxima Region is used as a feature to convert relative air volume to absolute air volume. Gradient volume is calculated using Photometric Stereo and then the gradient volume is converted to absolute volume by using two calibration steps which are also discussed in this chapter.

## **5.1 Calculating Absolute Amount of Air Volume**

Air volume calculated from photometric stereo in the section 3.3 does not give the absolute amount of air. To calculate the absolute amount of air from the surface gradient we use two calibration steps. The first calibration step is to convert the gradient information into digital flow value which is achieved through linear regression by constructing a feature vector of gradient, number of pixels and distance information. This digital flow value is then converted to absolute air volume in the second step by using a linear curve fitting of digital flow to a values carefully estimated from a Analog flow meter. The flow of data and calibration process is shown in Figure 5.1.

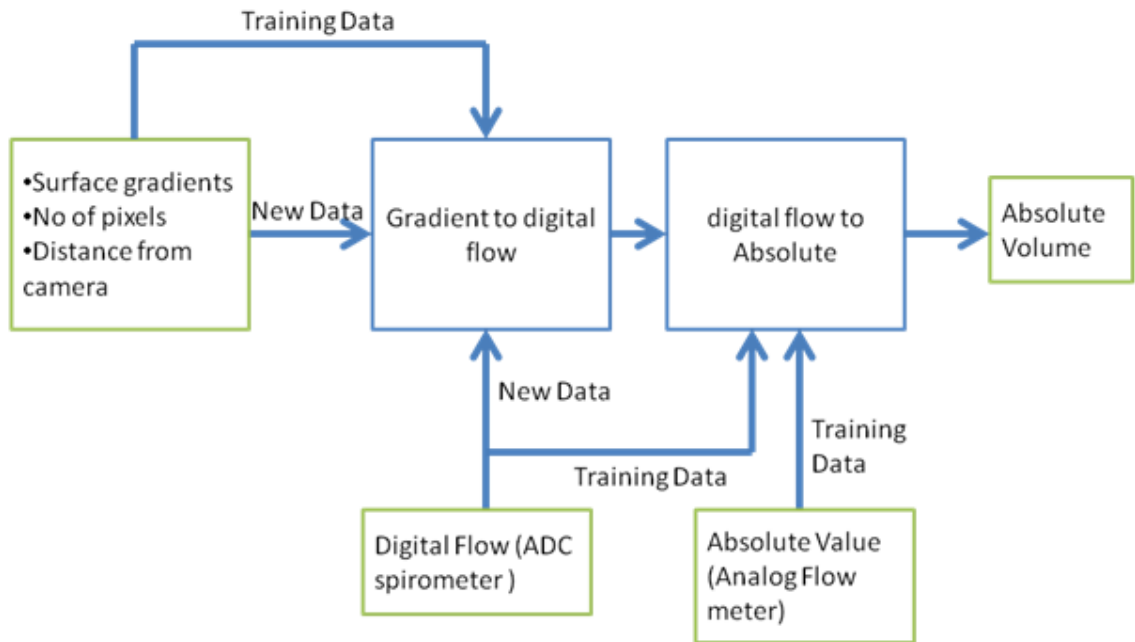


Figure 5.1: Gradient Volume to Absolute volume conversion

### 5.1.1 Gradient to digital flow

The least square method is used for regression by using a feature matrix  $[X]$ .  $[X]$  is constructed using the surface gradient, number of pixels and the distance of object from camera which is obtained through technique developed in last chapter. The signal obtained from the Pneumotachometer is digitized using an analog to digital converter (ADC) and is represented as  $p_v$ .  $\phi$  is trained using  $[X]$  and  $p_v$ . Five healthy subjects were used for training of  $\phi$ .

$$X = [\textit{gradient}, \textit{number of pixels}, \textit{distance}] \quad (5.1)$$

$$\phi = (X' * X)^{-1} * X' * pv \quad (5.2)$$

$$pv_2 = X_2 * \phi \quad (5.3)$$

Where  $[X_2]$  is the new input and  $pv_2$  is the synthesised digital Pneumotachometer signal which will be converted to absolute air volume using Equation 5.4.

### 5.1.2 Digital flow to absolute volume

The system attempts to measure the tidal breathing characteristics of a patient by optically measuring the volume of the torso. As a comparison, data are recorded synchronously from a pneumotachometer to benchmark the performance of the system against a current medical technique. A calibration experiment has been conducted to quantify the companion pneumotachometer data and hence evaluates the performance of the system.

The pneumotachometer used is a Hans Rudolph type 3700B, with a specified range of  $0 \rightarrow 2\frac{2}{3}$  L/s. The pneumotachometer itself is calibrated by the manufacturer in terms of input flow rate to output differential pressure, but multiple pieces

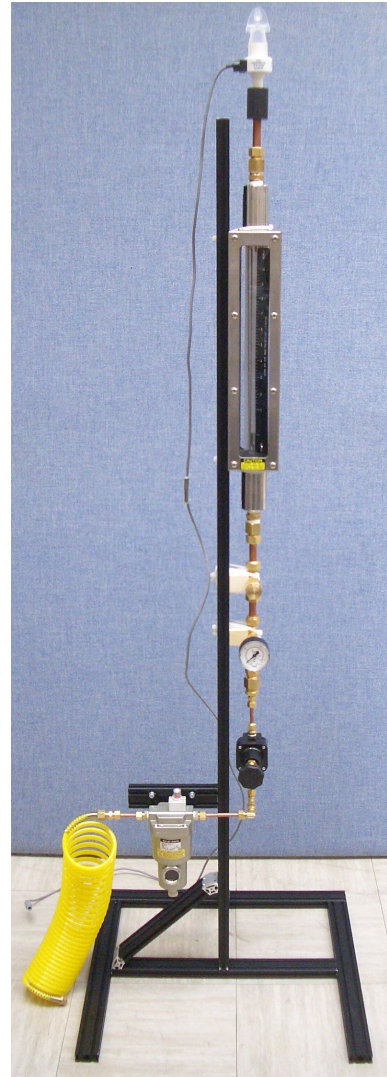
of instrumentation are required to measure the differential pressure. Therefore a wider calibration of the pneumotachometer system is required.

A pneumatic calibration system has been constructed to perform the calibration. An 8 standard atmosphere air compressor with a 24 litre tank provides the air source, followed by a  $0.01 \mu m$  filter to minimise oil contamination of the air. A manually operated precision pressure regulator provides the flow rate control. Air flow measurements are provided by an Omega FL911G rotameter type flowmeter, which measures flow rate up to  $10.2 \text{ ft}^3/\text{min}$  ( $4.8 \text{ l/s}$ ), with an accuracy of 2% of full scale, and repeatability of 1% of full scale. Flow measurements were performed with the compressor unpowered to prevent noise being introduced into the air flow. With careful control of the pressure regulator, it was possible to consistently achieve flow rates with a precision of  $0.05 \text{ ft}^3/\text{min}$  ( $24 \text{ ml/s}$ ), one quarter of the flowmeter's coarse scale marking of  $0.2 \text{ ft}^3 \text{ min}^{-1} / 0.2''$  ( $94 \text{ ml s}^{-1} / 5.1 \text{ mm}$ ).

The volume of the air tank was sufficient to allow approximately twenty seconds of constant flow rate at the maximum used flow setting ( $3 \text{ l/s}$ ), before the tank pressure dropped too low for the regulator to perform linearly. This allowed sufficient time to adjust the regulator settings to the desired flow rate and initiate measurements before moving on to the next flow setting. The equation (5.4) obtained after calibration is used to calculate the absolute amount of air as shown



(a) Air Compressor



(b) Pneumatic Rig

Figure 5.2: Pneumatic Apparatus

in section 5.1.2.

The absolute amount of air inhaled and exhaled is calculated from digital flow by using linear curve fitting. The coefficients of polynomial are calculated using values obtained from the carefully controlled air flow meter and then digitizing that flow using an analog to digital converter and a transducer.

$$absolutevolume = C_1 * pv_2 + C_0 \quad (5.4)$$

Where  $C_1 = 0.002085$ ,  $C_0 = -4.007$

## 5.2 Results

The mechanical and electrical components used for building the rigs have been approved as safe for use with human subjects. The setup has been used to test on six healthy volunteers with authorization of ethics approval. These six subjects are different from the five subjects used during training so a total of 11 subjects are used during the whole process.

The following experiments are designed to verify the accuracy of the developed PS imaging system and the performance for measuring the breath volume. A commercial 3D scanner and a pneumotachometer are being employed as a reference for comparing measurement results. To quantify the error of surface gradient obtained from photometric stereo, we compared it with gradient obtained from 3dMD [1], a commercial device with 0.2 mm accuracy in depth measurement. The results in Table 5.1 show the moderate errors associated with the PS approach which are acceptable when compared to those for the gradient obtained

from 3dMD system.

	Mean Angular Error (degree)	
	PS	3dMD
Synthetic Sphere	1.64	N/A
Real polystyrene Sphere	1.83	0.32
120 degree wedge	1.9	0.4

Table 5.1: Mean Angular Error in surface normal obtained using Photometric Stereo and 3dMD

A high correlation (0.98) between gradient volume and Pneumotachometer volume (Ground Truth) was found as shown in Figure 5.3. This also indicates that the effect of error in the surface gradient is very minimal following volume calculation, because of the normalization and calibration processes used to calculate the relative and absolute amount of air.

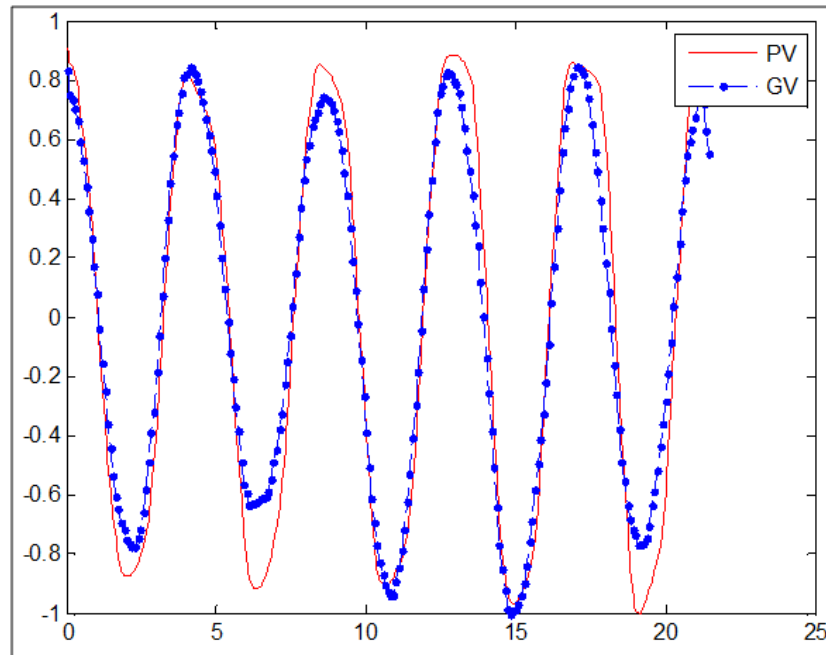


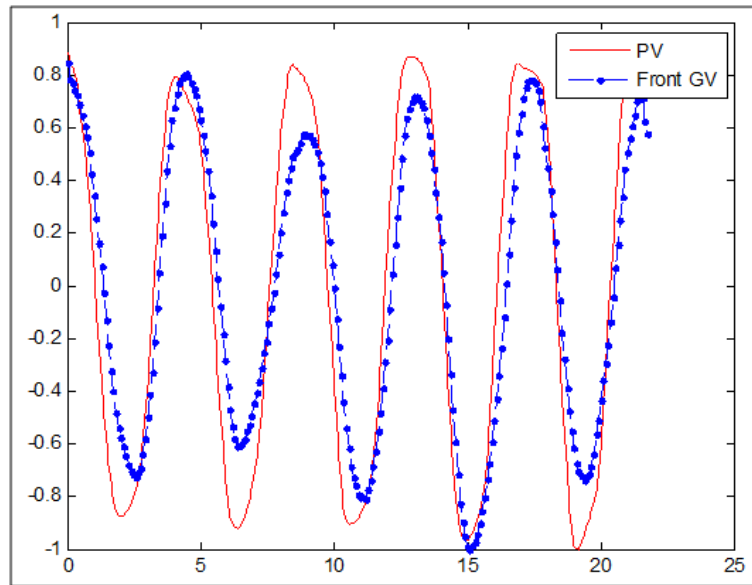
Figure 5.3: Comparison of Pneumotachometer Volume (PV) and Gradient Volume (GV) (combined front and back). Horizontal axis is time in seconds. Vertical scale is a normalized representation of volume.

Analysis of the front and back has been performed independently, which suggests that the correlation of the back gradient volume is negatively correlated to the Pneumotachometer volume and front gradient volume is positively correlated to Pneumotachometer volume as shown in Figure 5.4. The Front GV shows high correlation with PV. But when the back GV which is weakly and negatively correlated with PV, is added to front GV it yields higher correlation as compared to the front GV alone. This phenomenon is shown in Figure 5.4 as well as in Table 5.2.

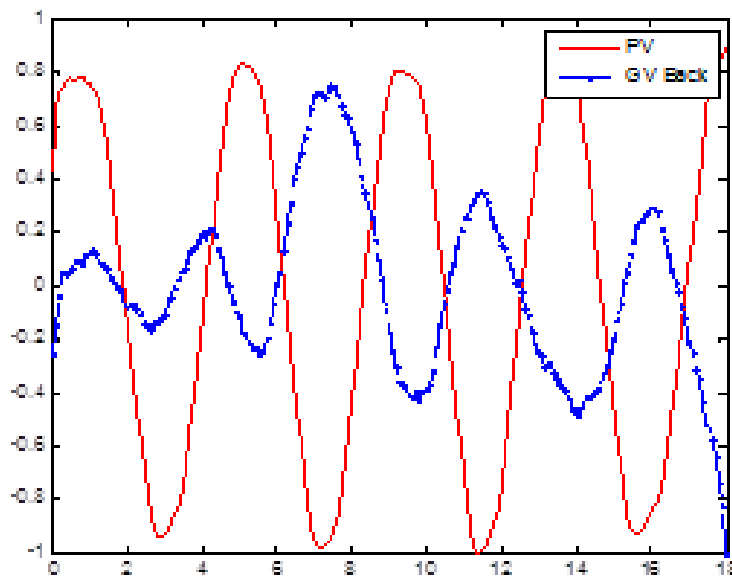
	Correlation
Front GV	0.94
Back GV	-0.64
Combined GV	0.98

Table 5.2: Gradient Volume analysis and comparison of front, back and combined

GV



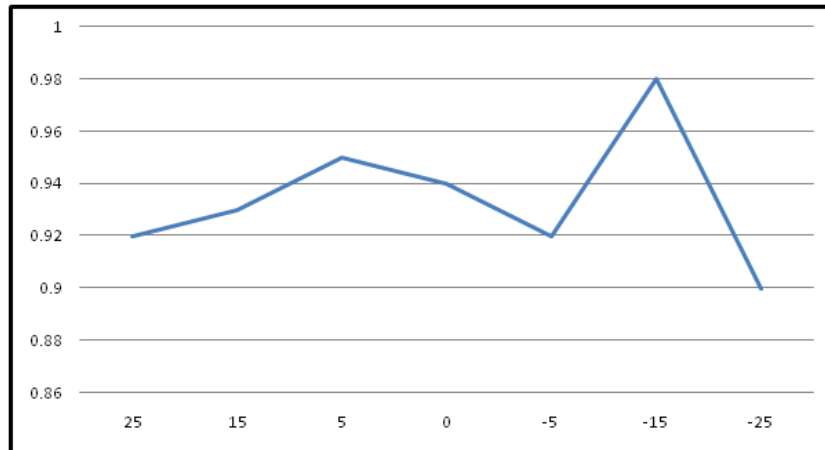
(a)



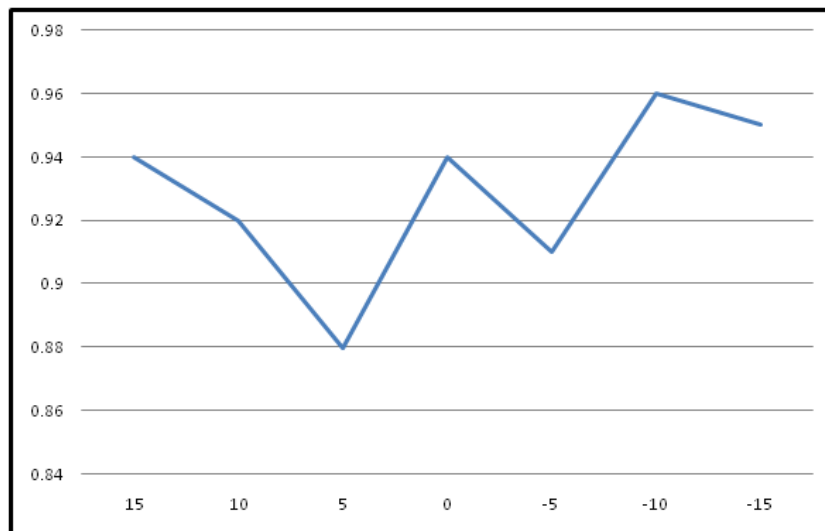
(b)

Figure 5.4: (a): front Gradient Volume (GV) and Pneumotachometer Volume (PV) plot, (b): back GV and PV plot. Horizontal axis is time in seconds. Vertical scale is a normalized representation of volume.

The system is also designed to be tolerant to the subject's position and orientation within the rig. Figure 5.5(a) and Figure 5.5(b) shows the correlation between the volume obtained from Pneumotachometer volume and gradient volume while the subject is standing in different locations relative to the rig. After the calibration process of converting the relative GV to absolute air volume the correlation drops from 0.98 to 0.96 as shown in Figure 5.6. This is due to errors introduced during the training and curve fitting processes involved in calibration steps.

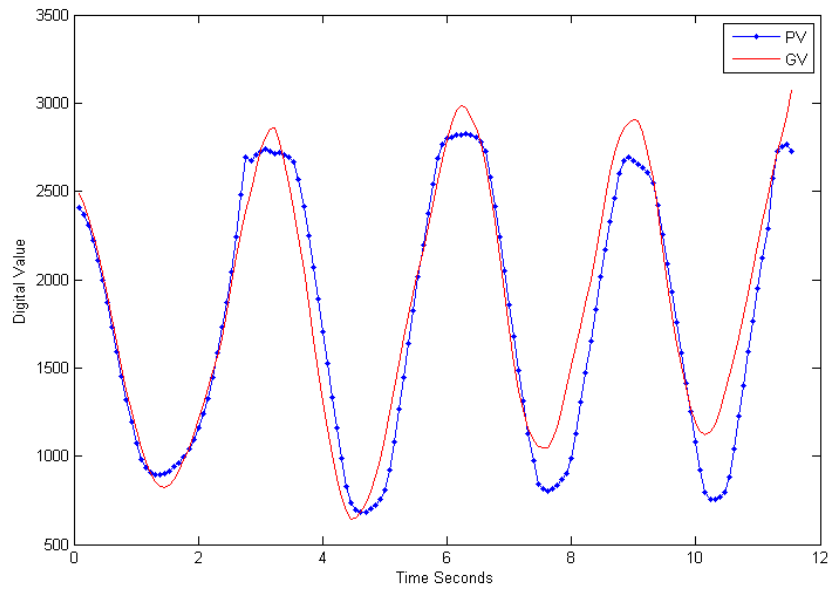


(a) Sagittal plane

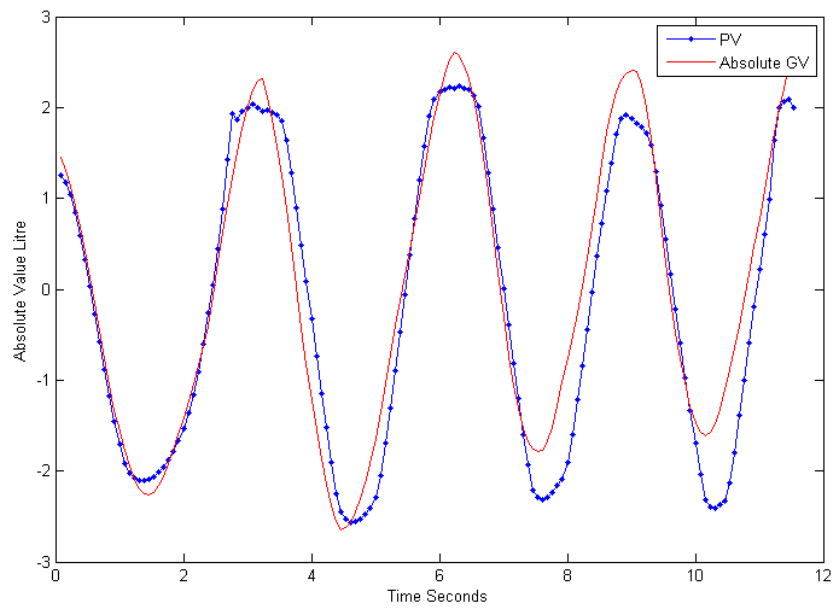


(b) Coronal plane

Figure 5.5: Subject displacement chart in Sagittal and Coronal plane. Vertical axis is the correlation between Gradient volume and Pneumotachometer volume. Horizontal axis is the displacement of subject from centre of rig in Sagittal and Coronal plane in centimeters.



(a)



(b)

Figure 5.6: (a) the plot of Pneumotachometer volume and Gradient volume in digital scale. (b) the plot of Pneumotachometer Volume and Gradient absolute volume in litres

The experiments have been performed on 6 healthy subjects and results have been summarised in Table 5.3. Table 5.3 shows high degree of correlation between the air volume obtained from a Pneumotachometer and the air volume estimated from photometric stereo images.

	Correlation between PV and Absolute GV
Subject 1	0.960
Subject 2	0.935
Subject 3	0.963
Subject 4	0.958
Subject 5	0.916
Subject 6	0.922

Table 5.3: Pseudo code of proposed method.

## 5.3 Conclusion

We have proposed a novel non-contact approach and designed a device to perform Pulmonary Functional Testing (PFT) on patients of any age. The unique features of the device are that it needs very little calibration and no registration between front and back view, and generates at least 2000 times higher resolution data compared to similar systems. We also presented a method to calculate the distance of a subject from a camera using photometric stereo images which helps

in calculating the absolute amount of air inhaled and exhaled. As the system is based on off the shelf and cheap components it is relatively easy and cheap to design. In the future we are planning to use the device for detecting a range of chest and back bone problems and take advantages of high resolution 3D recovery for regional analysis of the torso.

## **Chapter 6**

# **Conclusions, Limitations and Future Work**

Pulmonary functional tests are very essential in order to assess the lung functionality for many respiratory conditions and diseases, such as chronic obstructive pulmonary disease (COPD) and asthma. It also helps the patient with undiagnosed respiratory symptoms such as wheezing, coughing, or shortness of breath. However pulmonary functional testing is not always possible as it requires a high degree of compliance from the patient. This higher degree of compliance is not always possible from very young or very old patients. This test is also not feasible for an unconscious patient or someone who is not capable of holding mouth piece in their mouth.

Although a Spirometer provides very good data in relation to pulmonary functional testing, a Spirometer only gives two dimensional data and does not give any information about the physical structure of human chest or abdomen. It yields no information as to whether the patient is breathing from the chest or abdomen and whether both lungs are contributing equally to the in total breathing volume or not.

A photometric stereo based non-contact pulmonary functional testing is proposed in this thesis. The set-up is capable of capturing simultaneously, motion of the human torso both from front and back. Although the data acquisition of the front and the back is simultaneous, there is no registration required between both views. Only the front side can be used if patient is not capable of standing in the

rig. Even though the gradient volume obtained from back side is negatively correlated with ground truth, when combined with front gradient volume, it produces higher resultant correlation than the front only. This phenomenon has not been demonstrated by any other system designed for pulmonary functional testing before. Due to the use of the off-the-shelf camera and illumination sources, it is very inexpensive to physically build this system and a high spatial resolution can also be achieved with low cost consumer cameras.

A method to calculate the distance between the object and the camera, using photometric stereo images is presented in this thesis. This method also provides the ability to calculate the absolute amount of air inhaled and exhaled. This approach offers a useful way to add range data, improving accuracy and reducing distortion in Photometric Stereo acquired reconstructed 3D surfaces. Distortion in Photometric Stereo derived 3D surface data is a well known limitation of the method and its solution offers opportunity for taking advantage of the Photometric Stereo methodology in a new range of challenging applications, including accurate real-time reconstruction of non-rigid 3D surfaces, such as the moving human chest. In this thesis we also presented a new method to calculate light vectors dynamically for improving photometric stereo 3D surface reconstruction performance. The improvement in light vector estimation is achieved through cal-

culating the distance of the object from the camera, using diffused maxima region and then using this distance to calculate per-pixel light vector dynamically. This dynamic calculation can be done in real-time (i.e. real-time reconstruction of a deforming 3D shape, such as a human chest). By using the proposed method, the error in surface normal estimation is reduced to become almost constant and independent from the working distance. Experiments performed on synthetic and real scenes shows there is improvement of up to 45% in surface normal and up to 6 mm in the reconstructed surface height.

## **Limitations and Future Work**

A high correlation has been achieved between a Spirometer and the proposed method, however it does have its limitations.

The system currently requires a manual estimation of the initial pseudo light vector, with the help of a specular sphere. This step is performed to calculate the absolute distance of the object from the camera and to calculate the improved light vectors. This is only required once, when the rig is installed but a possible future work would be to automatically calculate these initial light vectors.

One of the main assumption of the system, is that all light sources emit homogeneous amount of light with respect to each other as well as with respect to the

area under observation. This assumption is not true for real physical light sources and can make a big difference in overall surface gradient calculation. Hence this could be investigated further to improve the system's accuracy.

The current size of the physical rig is not very practical for small examination rooms, so possible future work is to investigate the possibility of a smaller sized rig. The smaller size of the rig will have an additional advantage of a homogeneous distribution of light with respect to centre of the area of observation, as errors in light vector will be evenly distributed around the centre of the observed scene.

Currently, experiments and analysis are performed on healthy subjects with no known breathing conditions. However the non-contact nature of the device is ideal for doing breathing analysis of patients with many breathing related conditions. In addition to helping doctors with fast and accurate analysis of breathing conditions, it can also be used for monitoring chronic conditions. This method has potential for being a substitute for monitoring conditions like scoliosis; which is currently usually monitored using x-rays that have harmful side effects.

The method has been successfully calibrated and tested on healthy subjects, however the technique still needs to be tested on real patients on the ward. The calibration procedure used in this work can be further extended and applied to

different medical conditions and patients.

# References

- [1] 3dMD. [www.3dmd.com/3dmdface.html](http://www.3dmd.com/3dmdface.html).
- [2] J. Ackermann, F. Langguth, S. Fuhrmann, and M. Goesele. Photometric stereo for outdoor webcams. *IEEE Conference on Computer Vision and Pattern Recognition*, pages 262–269, June 2012.
- [3] J. Ahmad, J. Sun, L. Smith, and M. Smith. Novel Photometric Stereo Based Pulmonary Function Testing. In *3rd International Conference and Exhibition on 3D Body Scanning Technologies*, 2012.
- [4] A. Aliverti, R. Dellacà, and A. Pedotti. Optoelectronic plethysmography: a new tool in respiratory medicine. *Recenti Progressi in Medicina*, 92(11):644–7, November 2001.
- [5] A. Aliverti, R. Dellaca, P. Pelosi, D. Chiumello, A. Pedotti, and L. Gattinoni. Optoelectronic plethysmography in intensive care patients. *American Journal of Respiratory and Critical Care Medicine*, 161(5):1546–1552, May 2000.
- [6] A. Aliverti, K. Rodger, R. Dellacà, N. Stevenson, A. Lo Mauro, A. Pedotti, P. Calverley, and A. Mauro. Effect of salbutamol on lung function and chest

wall volumes at rest and during exercise in COPD. *Thorax*, 60(11):916–24, November 2005.

- [7] A. Aliverti, N. Stevenson, R. Dellaca, A. Mauro, A. Pedotti, and P. Calverley. Regional chest wall volumes during exercise in chronic obstructive pulmonary disease. *Thorax*, 59(3):210–216, March 2004.
- [8] R. Anderson, B. Stenger, and R. Cipolla. Color photometric stereo for multicolored surfaces. In *IEEE International Conference on Computer Vision*, pages 2182–2189, November 2011.
- [9] H. Aoki, K. Koshiji, H. Nakamura, Y. Takemura, and M. Nakajima. Study on respiration monitoring method using near-infrared multiple slit-lights projection. In *IEEE International Symposium on Micro-NanoMechatronics and Human Science*, pages 273–278, 2005.
- [10] H. Aoki, Y. Takemura, K. Mimura, and M. Nakajima. Development of non-restrictive sensing system for sleeping person using fiber grating vision sensor. In *IEEE International Symposium on Micromechatronics and Human Science*, pages 155–160, 2001.
- [11] I. Ashdown. Near-field photometry: Measuring and modeling complex 3-d light sources. *ACM SIGGRAPH95 Course Notes-Realistic Input for Realistic Images*, pages 1–15, 1995.
- [12] J. Askanazi, P. Silverberg, R. Foster, A. Hyman, J. Milic-Emili, and J. Kinney. Effects of respiratory apparatus on breathing pattern. *Journal of*

*Applied Physiology: Respiratory, Environmental and Exercise Physiology*, 48(4):577–80, April 1980.

- [13] J. Askanazi, P. Silverberg, A. Hyman, R. Foster, M. Yaremchuk, and J. Kinney. Effects of the mask and mouthpiece plus noseclip on spontaneous breathing pattern. *Critical Care Medicine*, 6(3):143–146, May 1978.
- [14] S. Barsky and M. Petrou. The 4-source photometric stereo technique for three-dimensional surfaces in the presence of highlights and shadows. *IEEE Transactions on Pattern Analysis and Machine Intelligence*, 25(10):1239–1252, October 2003.
- [15] F. Bastianini, S. Silvestri, G. Magrone, E. Gallotta, and S. Sterzi. A preliminary efficacy evaluation performed by opto-electronic plethysmography of asymmetric respiratory rehabilitation. In *Annual International Conference of the IEEE Engineering in Medicine and Biology Society. IEEE Engineering in Medicine and Biology Society.*, pages 849–52, January 2009.
- [16] P. Belhumeur, D. Kriegman, and A. Yuille. The Bas-Relief Ambiguity. *International Journal of Computer Vision*, 35(1):33–44, November 1999.
- [17] C. Bert and K. Metheany. A phantom evaluation of a stereo-vision surface imaging system for radiotherapy patient setup. *Medical Physics*, 32(9):2753–2762, 2005.
- [18] K. Bloch, J. Barandun, and M. Sackner. Effect of mouthpiece breathing on cardiorespiratory response to intense exercise. *American Journal of Respiratory and Critical Care Medicine*, 151(4):1087–92, April 1995.

- [19] N. Borghese and G. Ferrigno. An algorithm for 3-D automatic movement detection by means of standard TV cameras. *IEEE Transactions on Biomedical Engineering*, 37(12):1221–1225, December 1990.
- [20] S. Cala, C. Kenyon, G. Ferrigno, P. Carnevali, A. Aliverti, A. Pedotti, P. Macklem, and D. Rochester. Chest wall and lung volume estimation by optical reflectance motion analysis. *Journal of Applied Physiology*, 81(6):2680–2689, December 1996.
- [21] J. Clark. Active photometric stereo. In *IEEE Computer Society Conference on Computer Vision and Pattern Recognition*, pages 29–34, June 1992.
- [22] R. Cook and K. Torrance. A reflectance model for computer graphics. *ACM Transactions on Graphics*, 1(1):7–24, 1982.
- [23] W. de Boer, J. Lasenby, J. Cameron, R. Wareham, S. Ahmad, C. Roach, W. Hills, and R. Iles. SLP: A Zero-Contact Non-Invasive Method for Pulmonary Function Testing. In *British Machine Vision Conference*, pages 85.1–85.12, 2010.
- [24] B. De Decker, J. Kautz, T. Mertens, and P. Bekaert. Capturing multiple illumination conditions using time and color multiplexing. In *IEEE Conference on Computer Vision and Pattern Recognition*, pages 2536–2543, June 2009.
- [25] R. Dellaca, M. Ventura, and E. Zannin. Measurement of total and compartmental lung volume changes in newborns by optoelectronic plethysmography. *Pediatric Research*, 67(1):11–16, January 2010.

- [26] H. Du, D. Goldman, and S. Seitz. Binocular Photometric Stereo. In *British Machine Vision Conference*, pages 84.1–84.11, 2011.
- [27] F. Dunn and I. Parberry. *3D math primer for graphics and game development*. Wordware Publishing, Inc, 2011.
- [28] D. Falie and M. Ichim. Sleep monitoring and sleep apnea event detection using a 3D camera. In *8th International Conference on Communications*, pages 177–180, 2010.
- [29] P. Favaro and T. Papadhimetri. A closed-form solution to uncalibrated photometric stereo via diffuse maxima. In *IEEE Conference on Computer Vision and Pattern Recognition*, pages 821–828, June 2012.
- [30] G. Ferrigno and A. Pedotti. ELITE: a digital dedicated hardware system for movement analysis via real-time TV signal processing. *IEEE Transactions on Biomedical Engineering*, 32(11):943–950, November 1985.
- [31] P. Fregadolli and A. Sasseron. Comparison between the use of mouthpiece and facemask in assessing lung volumes and vital capacity in healthy subjects. *Fisioterapia e Pesquisa*, 2010.
- [32] G. Fyffe, X. Yu, and P. Debevec. Single-shot photometric stereo by spectral multiplexing. In *IEEE International Conference on Computational Photography*, 2011.
- [33] O. Georgiadou, I. Vogiatzis, G. Stratakos, A. Koutsoukou, S. Golemati, A. Aliverti, C. Roussos, and S. Zakyntinos. Effects of rehabilitation on chest

wall volume regulation during exercise in COPD patients. *The European Respiratory Journal*, 29(2):284–291, February 2007.

- [34] D. Gierga, J. Turcotte, G. Sharp, S. Jiang, K. Doppke, A. Katz, A. Taghian, and G. Chen. Target registration error with three-dimensional surface imaging in setup of image-guided partial breast irradiation. *International Journal of Radiation Oncology Biology Physics*, 63(1):S536–S537, 2005.
- [35] R. Gilbert and J. Auchincloss. Changes in tidal volume, frequency, and ventilation induced by their measurement. *Journal of Applied Physiology*, 33(2):252–254, 1972.
- [36] J. Han, K. Stegen, M. Cauberghs, and K. Van de Woestijne. Influence of awareness of the recording of breathing on respiratory pattern in healthy humans. *European Respiratory Journal*, 10(1):161–166, January 1997.
- [37] M. Hansen, G. Atkinson, L. Smith, and M. Smith. 3D face reconstructions from photometric stereo using near infrared and visible light. *Computer Vision and Image Understanding*, 114(8):942–951, August 2010.
- [38] C. Hern, G. Vogiatzis, and C. Hernández. Self-calibrating a real-time monocular 3d facial capture system. In *International Symposium on 3D Data Processing, Visualization and Transmission*, 2010.
- [39] C. Hernández, G. Vogiatzis, and R. Cipolla. Multiview photometric stereo. *IEEE Transactions on Pattern Analysis and Machine Intelligence*, 30(3):548–554, March 2008.

- [40] C. Hernández, G. Vogiatzis, and R. Cipolla. Shadows in three-source photometric stereo. *Lecture Notes in Computer Science (including subseries Lecture Notes in Artificial Intelligence and Lecture Notes in Bioinformatics)*, 2008.
- [41] C. Hernández, G. Vogiatzis, and R. Cipolla. Overcoming shadows in 3-source photometric stereo. *IEEE Transactions on Pattern Analysis and Machine Intelligence*, 33(2):419–26, February 2011.
- [42] T. Higo, Y. Matsushita, N. Joshi, and K. Ikeuchi. A hand-held photometric stereo camera for 3-D modeling. In *12th International Conference on Computer Vision*, pages 1234–1241, September 2009.
- [43] I. Horowitz and N. Kiryati. Depth from gradient fields and control points: Bias correction in photometric stereo. *Image and Vision Computing*, 22(9):681–694, August 2004.
- [44] Y. Iwahori, H. Sugie, and N. Ishii. Reconstructing shape from shading images under point light source illumination. In *10th International Conference on Pattern Recognition*, volume i, pages 83 –87, June 1990.
- [45] U. Johnson, D. Landau, and J. Lindgren-Turner. Real time 3D surface imaging for the analysis of respiratory motion during radiotherapy. *Journal of Radiation*, 60(1):S603–S604, 2004.
- [46] A. Jones, G. Fyffe, X. Yu, Wan-Chun C Ma, J. Busch, R. Ichikari, M. Bolas, and P. Debevec. Head-Mounted Photometric Stereo for Performance Cap-

- ture. In *Conference for Visual Media Production*, pages 158–164, November 2011.
- [47] D. Junyu, G. McGunnigle, S. Liyuan, F. Yanxia, and W. Yuliang. Improving photometric stereo with laser sectioning. In *12th IEEE International Conference on Computer Vision Workshops*, pages 1748–1754, 2009.
- [48] B. Kim and P. Burger. Depth and shape from shading using the photometric stereo method. *Image Understanding*, 54(3):416–427, 1991.
- [49] M. Kobayashi, T. Okabe, Y. Matsushita, and Y. Sato. Surface Reconstruction in Photometric Stereo with Calibration Error. In *International Conference on 3D Imaging, Modeling, Processing, Visualization and Transmission*, pages 25–32. Inst. of Ind. Sci., Univ. of Tokyo, Tokyo, Japan, May 2011.
- [50] T. Kondo, T. Uhlig, P. Pemberton, and P. Sly. Laser monitoring of chest wall displacement. *European Respiratory Journal*, 10(8):1865–1869, August 1997.
- [51] R. Kozera and L. Noakes. Noise reduction in photometric stereo with non-distant light sources. *Computer Vision and Graphics*, 32:103–110, 2006.
- [52] A. Layton, S. Moran, C. Garber, H. Armstrong, R. Basner, B. Thomashow, and M. Bartels. Optoelectronic plethysmography compared to spirometry during maximal exercise. *Respiratory physiology & neurobiology*, 185(2):362–368, January 2013.
- [53] ANZAI Medical Co. Ltd. <http://www.anzai-med.co.jp>.

- [54] Orange Tree Technologies Ltd. ZestSC1 FPGA board.
- [55] Vision RT Ltd. <http://www.visionrt.com/>.
- [56] Z. Lu, Y. Tai, M. Ben-Ezra, and M. S. Brown. A framework for ultra high resolution 3D imaging. In *IEEE Computer Society Conference on Computer Vision and Pattern Recognition*, pages 1205–1212, June 2010.
- [57] R. Mecca, G. Rosman, R. Kimmel, and A. Bruckstein. Perspective Photometric Stereo with Shadows. In *Scale Space and Variational Methods in Computer Vision*, pages 258–269. Springer, 2013.
- [58] R. Mecca, A. Wetzler, R. Kimmel, and A. Bruckstein. Direct Shape Recovery from Photometric Stereo with Shadows. In *International Conference on 3D Vision*, pages 382–389, 2013.
- [59] D. Miller, E. Klein, I. Zoberi, M. Taylor, and S. Powell. Inter-fraction and Intra-fraction Breast Motion Localized using AlignRT for Early Breast Cancer. *International Journal of Radiation Oncology Biology Physics*, 72(1):S189–S190, 2008.
- [60] B. Mityashev. The scattering of electromagnetic waves from rough surfaces. *USSR Computational Mathematics and Mathematical Physics*, 4(6):247–249, January 1964.
- [61] K. Müller, C. Schaller, J. Penne, and J. Hornegger. Surface-Based Respiratory Motion Classification and Verification. *Bildverarbeitung für die Medizin*, 2009.

- [62] J. Penne, C. Schaller, J. Hornegger, and T. Kuwert. Robust real-time 3D respiratory motion detection using time-of-flight cameras. *International Journal of Computer Assisted Radiology and Surgery*, 3(5):427–431, July 2008.
- [63] K. Povšič, M. Fležar, J. Možina, and M. Jezeršek. Laser 3-D measuring system and real-time visual feedback for teaching and correcting breathing. *Journal of Biomedical Optics*, 17(3):036004–1–036004–8, March 2012.
- [64] S. Powell, K. Doppke, and G. Chen. Set-up uncertainty in accelerated partial-breast irradiation using 3D-conformal external beam radiotherapy: A companion study to a prospective phase I ongoing trial. *Journal of Radiation*, 60(1):S400–S401, 2004.
- [65] R. Schlegelmilch and R. Kramme. Pulmonary Function Testing. In *Springer Handbook of Medical Technology*, pages 95–117. Springer Berlin Heidelberg, 2011.
- [66] C. Schlick. An Inexpensive BRDF Model for Physically-based Rendering. *Computer Graphics Forum*, 13(3):233–246, 1994.
- [67] T. Simchony, R. Chellappa, and M. Shao. Direct analytical methods for solving Poisson equations in computer vision problems. *IEEE Transactions on Pattern Analysis and Machine Intelligence*, 12(5):435–446, 1990.
- [68] L. Smith and M. Smith. The virtual point light source model the practical realisation of photometric stereo for dynamic surface inspection. In *13th international conference on Image Analysis and Processing, ICIAP'05*, pages 495–502, 2005.

- [69] M. Smith and L. Smith. Dynamic photometric stereo—a new technique for moving surface analysis. *Image and Vision Computing*, 23(9):841–852, September 2005.
- [70] J. Sun, M. Smith, L. Smith, and A. Farooq. Examining the uncertainty of the recovered surface normal in three light photometric stereo. *Image and Vision Computing*, 25(7):1073–1079, 2007.
- [71] J. Sun, M. Smith, L. Smith, S. Midha, and J. Bamber. Object surface recovery using a multi-light photometric stereo technique for non-Lambertian surfaces subject to shadows and specularities. *Image and Vision Computing*, 25(7):1050–1057, 2007.
- [72] K. Tan, R. Saatchi, H. Elphick, and D. Burke. Real-time vision based respiration monitoring system. In *7th International Symposium on Communication Systems Networks and Digital Signal Processing*, pages 770–774. IEEE, 2010.
- [73] S. Tsujimura and H. Nakamura. Evaluation of a new fiber-grating vision sensor for assessing pulmonary functions in healthy and COPD subjects. *Physiological Measurement*, 32(10):1701–1713, 2011.
- [74] A. Varnavas, V. Argyriou, J. Ng, and A. Bharath. Dense photometric stereo reconstruction on many core GPUs. In *IEEE Computer Society Conference on Computer Vision and Pattern Recognition - Workshops*, pages 59–65, June 2010.
- [75] A. Vasquez, T. Moser, G. Echner, G. Sroka-Perez, and CP Karger. Inves-

- tigation of a stereoscopic camera system for gated radiotherapy. In *World Congress on Medical Physics and Biomedical Engineering*, pages 315–317. Springer, 2009.
- [76] G. Vogiatzis and C. Hernández. Self-calibrated, Multi-spectral Photometric Stereo for 3D Face Capture. *International Journal of Computer Vision*, 97(1):91–103, August 2011.
- [77] C. Voscopoulos, J. Brayanov, and D. Ladd. Evaluation of a Novel Noninvasive Respiration Monitor Providing Continuous Measurement of Minute Ventilation in Ambulatory Subjects in a Variety of Clinical. *Anesthesia and Analgesia*, 117(1):91–100, 2013.
- [78] Jack Wanger. *Pulmonary-function testing : A practical approach*. Jones & Bartlett Publishers, 2011.
- [79] G. Ward. Measuring and modeling anisotropic reflection. *ACM SIGGRAPH Computer Graphics*, 26(2):265–272, 1992.
- [80] Eric W. Weisstein. Divergence Theorem. *MathWorld – A Wolfram Web Resource (Last accessed 1 May 2012)*, 2011.
- [81] P. Western and J. Patrick. Effects of focusing attention on breathing with and without apparatus on the face. *Respiration Physiology*, 72(1):123–130, 1988.
- [82] R. Woodham. Photometric method for determining surface orientation from multiple images. *Optical Engineering*, 19(1):139–144, 1980.

- [83] C. Wu, Y. Liu, Q. Dai, and B. Wilburn. Fusing multiview and photometric stereo for 3D reconstruction under uncalibrated illumination. *IEEE Transactions on Visualization and Computer Graphics*, 17(8):1082–1095, August 2011.
- [84] L. Zhang, B. Curless, and S.M. Seitz. Rapid shape acquisition using color structured light and multi-pass dynamic programming. In *First International Symposium on 3D Data Processing Visualization and Transmission*, pages 24–36, 2002.